POLITECNICO DI TORINO
Repository ISTITUZIONALE

MXene-modified BiVO4/FePO4 photoanodes for solar oxygen evolution

Original
MXene-modified BiVO4/FePO4 photoanodes for solar oxygen evolution / Pozzati, M., Deriu, C., Ragonese, P., Cattelan, M., Lamberti, F., Zahorodna, V., Ihnatenko, Y., Altieri, R., Dukhnovskiy, S., Baginskiy, I., Gogotsi, O., Poli, I., Fabris, L., Gatti, T., Wang, M.. - In: NANOSCALE ADVANCES. - ISSN 2516-0230. - 8:20(2026), pp. 5890-5907. [10.1039/d6na00469e]

Availability:
This version is available at: 11583/3014836 since: 2026-08-25T08:56:25Z

Publisher:
Royal Society of Chemistry - RSC

Published
DOI:10.1039/d6na00469e

Terms of use:

This article is made available under terms and conditions as specified in the corresponding bibliographic description in the repository

Publisher copyright

(Article begins on next page)

29 November 2026

Nanoscale Advances

ROYAL SOCIETY OF CHEMISTRY

PAPER

Published on 18 August 2026
Licensed under CC-BY 4.0

Check for updates

Cite this: *Nanoscale Adv.*, 2026, **8**, 5890

MXene-modified $BiVO_4/FePO_4$ photoanodes for solar oxygen evolution

Micaela Pozzati,[a] Chiara Deriu,[a] Paola Ragonese,[b] Francesco Lamberti,[c] Mattia Cattelan,[c] Veronika Zahorodna,[de] Roberto Altieri,[f] Yana Ihnatenko,[e] Serhii Dukhnovskiy,[de] Ivan Baginskiy,[de] Oleksiy Gogotsi,[de] Isabella Poli,[b] Laura Fabris,[a] Teresa Gatti *[af] and Mengjiao Wang *[a]

Photoelectrochemical reactions in aqueous systems represent a promising route for solar fuel production; however, their efficiency is often constrained by the sluggish kinetics of the anodic oxygen evolution reaction (OER). $BiVO_4$ is one of the most promising photoanode materials and has demonstrated the ability to efficiently convert light into electrical and then chemical energy. However, the conversion efficiency of pure $BiVO_4$ remains insufficient. In this work, $BiVO_4$ photoanodes are first modified with $FePO_4$ using a simple Autodrop process and subsequently integrated with $Ti_3C_2T_x$ MXene overlayers deposited *via* automated spray coating. The thus modified photoanodes exhibit a superior performance thanks to the synergistic interaction between the $FePO_4$ and MXene layers, which promotes the movement of electrons and efficient charge separation, thus suppressing surface recombination in $BiVO_4$. Meanwhile, both the $FePO_4$ and MXene layers can act as hole-transport channels and co-catalytic interfaces, facilitating interfacial charge transfer and accelerating OER kinetics. Importantly, achieving an optimal balance between MXene coverage and $FePO_4$ exposure is critical to maximizing catalytic activity within the $BiVO_4/FePO_4$/MXene heterostructure. By optimizing the MXene loading, the modified $BiVO_4/FePO_4$ photoelectrode exhibits an approximately 50% improvement in photocurrent performance. Overall, this work presents a simple and effective strategy for fabricating high-performance photoanodes with potential for scalable production. The proposed heterojunction design provides a promising pathway toward the development of efficient and stable photoanodes for solar fuel applications.

Received 4th June 2026
Accepted 7th August 2026

DOI: 10.1039/d6na00469e

rsc.li/nanoscale-advances

1 Introduction

Photoelectrochemical (PEC) reactions offer a promising approach for the sustainable and environmentally friendly conversion of solar and electric energy into renewable fuels.[1,2] However, the overall efficiency of aqueous PEC systems is severely limited by the intrinsically sluggish kinetics of the anodic oxygen evolution reaction (OER). This bottleneck has motivated extensive research into the development of efficient and stable photoanode materials.[3] Among the various candidates, $BiVO_4$ has emerged as one of the most extensively studied photoanodes for the OER, owing to its good chemical stability in mild pH aqueous solution, optimal band gap (2.4–2.6 eV) for solar light absorption, and a suitable valence band position for the OER, allowing a theoretical photocurrent density of approximately 7.5 mA cm^{-2} to be reached.[4–7] Despite these advantages, the practical performance of $BiVO_4$ remains far below its theoretical limit due to several inherent drawbacks, including poor charge transport properties, severe surface recombination and photo-corrosion under operating conditions.[8] Therefore, surface and interface engineering strategies are often required to improve charge separation and interfacial charge transfer in $BiVO_4$-based photoanodes. To address these limitations, a variety of co-catalysts and surface modifiers have been explored, such as Al_2O_3, CoPi, Co_3O_4, NiB alloys, and FeOOH.[4,9–12] Among these surface modifiers, Fe-based compounds are particularly attractive due to the earth-abundant and non-critical nature of iron, as well as its well established role as an efficient active site for the OER. Furthermore, Fe-based layers provide surface passivation, mitigating surface defect states that otherwise would act as

[a]*Department of Applied Science and Technology, Politecnico di Torino, C.so Duca degli Abruzzi 24, 10129 Torino, Italy*

[b]*Center for Sustainable Future Technologies, Istituto Italiano di Tecnologia, Via Livorno 60, 10144 Torino, Italy*

[c]*Dipartimento di Scienze Chimiche, Università degli Studi di Padova, Via Marzolo, 1, 35131, Padova, Italy*

[d]*Materials Research Centre, 3 Krzhizhanovskogo Str., 03142 Kyiv, Ukraine*

[e]*Y-Carbon Ltd, 18 Bohdana Havrylyshyna st, Kyiv, Ukraine*

[f]*Center for Materials Research, Justus-Liebig University Giessen, Heinrich-Buff-Ring 16-17, 35392 Giessen, Germany. E-mail: teresa.gatti@polito.it; mengjiao.wang@polito.it*

© 2026 The Author(s). Published by the Royal Society of Chemistry

recombination centres.[4,13–15] Materials like $FePO_4$ can also function as a hole-transport layer, improving the effective hole transfer.[16]

Recently, two-dimensional conductive materials such as MXenes have emerged as promising interfacial modifiers for semiconductor photoelectrodes due to their high electrical conductivity and large surface area. 2D MXene materials, which are transition metal carbides, nitrides, or carbonitrides, have emerged as promising hole-transport and co-catalytic materials for PEC applications.[17] MXenes exhibit a unique combination of properties such as high electrical conductivity, hydrophilicity, tunable surface chemistry and high electronegativity, making them attractive for electrochemical and photoelectrochemical systems.[18] Among them, $Ti_3C_2T_x$, typically derived from the etching of the MAX phase Ti_3AlC_2, exhibits high surface reactivity due to abundant surface terminations such as –OH and –F groups, which facilitate interfacial interactions and functionalization.[19,20] As a result, MXenes have increasingly been explored as co-catalysts in PEC water splitting.[21–23] In the context of the OER, $BiVO_4$/MXene heterostructures have demonstrated enhanced activity and stability through improved charge transfer and suppressed recombination.[24,25] For instance, Jahangir *et al.* reported a $Ti_3C_2T_x/BiVO_4$ heterojunction achieving a photocurrent density of 4.72 mA cm^{-2},[17] which is 1.5 times higher than the photocurrent of pure $BiVO_4$, and Cheng *et al.* achieved 5.13 mA cm^{-2} using an alkaline-etched $BiVO_4$/MXene system.[26] In these systems, MXenes act as hole-extraction layers and conductive bridges, reducing series resistance, suppressing charge recombination, and accelerating interfacial charge transfer.[27] Although these studies demonstrate the promise of MXene-functionalized $BiVO_4$ photoanodes, most reported fabrication approaches remain limited to laboratory-scale methods, restricting their potential for large-scale production.[28,29]

In the practical development of modified $BiVO_4$ photoanodes, material optimization alone is insufficient; scalability and compatibility with industrial manufacturing should be considered equally critical. Moreover, thin-film fabrication techniques play a decisive role in tailoring the optical and electronic properties of photoanodes, thereby strongly influencing PEC performance. Established methods such as electrodeposition and spray pyrolysis have been widely employed for the fabrication of $BiVO_4$-based photoanodes, offering good control over film morphology and enabling significant performance improvements in modified architectures. Recent studies have highlighted their effectiveness in producing high-quality photoactive layers and in integrating cocatalysts or surface modifiers for enhanced PEC activity.[30–33] However, these techniques may require precise process control, elevated processing temperatures, or multiple post-treatment steps, which can complicate large-scale implementation, particularly for multilayered heterostructures. Conventional synthesis routes for $BiVO_4$-based heterostructures, such as hydrothermal methods, are often limited in scalability and reproducibility.[29,34,35] In contrast, the Autodrop technique, derived from the successive ionic layer adsorption and reaction (SILAR) process, offers a scalable and highly controllable approach for fabricating uniform $BiVO_4$-based photoanodes.[36,37] Our previous work has demonstrated the successful preparation of $BiVO_4/FePO_4$ photoanodes using the Autodrop method.[16,38] Additionally, automated spray coating has been introduced as an efficient strategy for depositing $Ti_3C_2T_x$ MXene films. This technique enables superior film uniformity, reduced electrical resistance, faster processing, and lower MXene consumption, making it particularly compatible for scalable electrode fabrication.[39,40] In addition to improving photoelectrode performance, the potential for scalable and controllable deposition methods remains an important aspect for practical implementation of PEC materials.

Building on these advances, combining the Autodrop process with automated spray coating offers a promising route to fabricate $BiVO_4/FePO_4$/MXene photoanodes with the possibility of scaling up. Here, we explore the combined use of an $FePO_4$ interlayer and MXene nanosheets to create complementary charge-transfer pathways within the photoanode architecture. In this work, $BiVO_4/FePO_4$ photoanodes were modified with $Ti_3C_2T_x$ MXene nanosheets using an automated spray-coating process. $BiVO_4/FePO_4$ photoanodes were first prepared *via* the Autodrop method, as previously reported by our group,[16,38] followed by the deposition of exfoliated $Ti_3C_2T_x$ MXene layers using automated spray coating with 1 mg mL^{-1} $Ti_3C_2T_x$ MXene colloidal solution (Fig. 1). By systematically varying the MXene loading, the influence of MXene film thickness on PEC performance is investigated. The optimized $BiVO_4$/

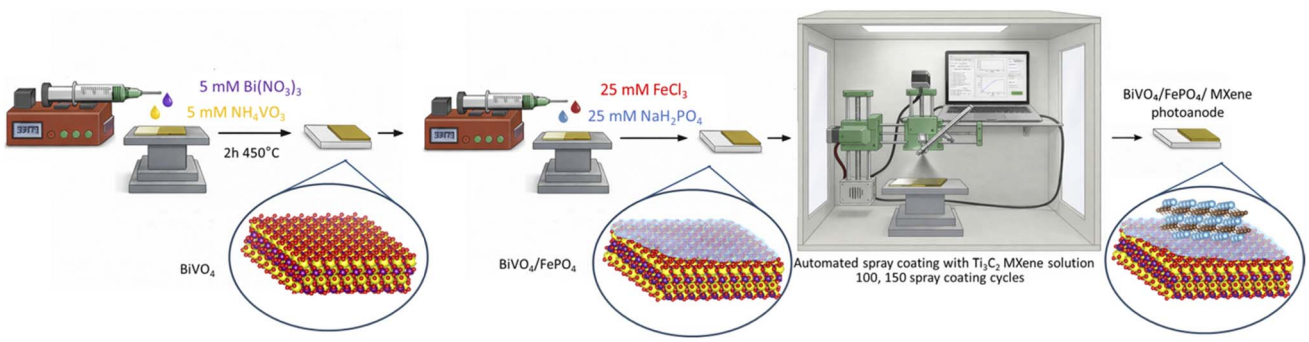

Fig. 1 Schematic representation of the Autodrop-spray coating processes used in this work to obtain $BiVO_4/FePO_4$/MXene photoanodes.

© 2026 The Author(s). Published by the Royal Society of Chemistry

$FePO_4$/MXene photoanode exhibits significantly enhanced PEC water oxidation performance, arising from improved bulk charge separation at the $BiVO_4/FePO_4$ junction and efficient charge transport and co-catalytic OER activity provided by the highly conductive $Ti_3C_2T_x$ MXene. Furthermore, the MXene overlayer enhances photoanode stability under PEC conditions by facilitating continuous hole extraction from the $BiVO_4$ semiconductor and preventing its degradation. This work demonstrates a viable strategy for the production of stable and high-performance $BiVO_4/FePO_4$/MXene photoanodes for PEC OER applications.

2 Experimental section

2.1 Materials

Bismuth(III) nitrate pentahydrate ($Bi(NO_3)_3 \cdot 5H_2O$), ammonium vanadate (NH_4VO_3), sodium dihydrogen phosphate (NaH_2PO_4), and iron chloride ($FeCl_3$) were acquired from Thermo Fisher. FTO-coated glass substrates were purchased from Sigma-Aldrich. Titanium aluminium carbide (Ti_3AlC_2) was obtained from Materials Research Center Ltd. Hydrofluoric acid (HF) was purchased from Honeywell, and hydrochloric acid (HCl) and lithium fluoride (LiF) were acquired from Roth.

2.2 Preparation of photoanodes

2.2.1 Autodrop of $BiVO_4$ and $FePO_4$ layers. The photoanodes were prepared by a procedure already published in our recent work with proof of reproducibility.[16] $BiVO_4$ was synthesized by dispensing a precursor solution containing 5 mM NH_4VO_3 and 5 mM $Bi(NO_3)_3 \cdot 5H_2O$ onto an FTO glass substrate using a KLM spin-coater SCV-10 (Fig. 1). The deposition was carried out using a syringe pump at a dispensing rate of 100 μL min^{-1} and a spinning speed of 40 rps, with a total deposited volume of 2 mL. After deposition, the substrate was annealed at 450 °C for 2 h using a heating ramp of 10 °C min^{-1}. $FePO_4$ was prepared by the Autodrop method as well, using 25 mM $FeCl_3$ and 25 mM NaH_2PO_4 as precursor solutions. The deposition parameters were a dispensing rate of 100 μL min^{-1}, a spinning speed of 40 rps, and a total deposited volume of 0.4 mL. The obtained films were subsequently annealed at 450 °C for 2 h with a heating ramp of 10 °C min^{-1}. The substrate area coated with the active material was 1 × 1 cm^2.

2.2.2 Exfoliation of MXene and automatic spray-coating of MXene layers. The procedure for MXene flake synthesis followed the one from an already published study.[41] $Ti_3C_2T_x$ MXene was prepared by selective etching of Ti_3AlC_2 in HF formed *in situ*, followed by repeated washing with Milli-Q water and centrifugation to remove residual acid and obtain multilayered $Ti_3C_2T_x$. Single- or few-layer $Ti_3C_2T_x$ MXene was then prepared using a minimally intensive layer delamination (MILD) procedure, in which Ti_3AlC_2 was etched in a LiF/HCl solution and the resulting suspension was washed and centrifuged until a dark supernatant containing delaminated MXene flakes was obtained. Collected supernatant was centrifuged at 3000 rcf for 20 minutes to sediment $Ti_3C_2T_x$. The collected sediment was washed several times to remove residual acid and LiF. The obtained $Ti_3C_2T_x$ MXene water based sediment was diluted with DI-water to form a 1 mg mL^{-1} $Ti_3C_2T_x$ suspension that was later on used for the automated spray coating procedure to deposit MXene flakes on top of the $BiVO_4$ and $BiVO_4/FePO_4$ photoanodes. $Ti_3C_2T_x$ MXene layers were deposited *via* cycles of short exposure of $BiVO_4/FePO_4$ photoanodes to an aerosol of a water-based $Ti_3C_2T_x$ colloidal solution. In the automated spray-coating process, one deposition cycle consisted of a slow pass of the spray nozzle across the electrode surface (≈1.5 s), followed by a return pass (≈1.5 s) and a short ambient drying period of about 1 s. Two sets of $BiVO_4/FePO_4$/MXene photoanodes were produced that were exposed to 100 and 150 such cycles. The automated spray-coating setup allows programmable control of deposition parameters and deposition cycles, enabling reproducible coating conditions and providing a practical route toward scalable fabrication of MXene-modified photoelectrodes. Pictures of the automated spray coating system are shown in the SI (Fig. S1).

2.3 Materials characterization

Scanning electron microscopy (SEM) images were recorded using a TESCAN SEM with an acceleration voltage of 5 kV, a beam current of 100 pA and a sensor to acquire and analyze the energy-dispersive X-ray spectra (EDS). Diffractogram spectra were acquired on a Malvern PANalytical Empyrean Series-3 diffractometer (Cu Kα radiation, Malvern Panalytical Ltd) at 40 kV and 40 mA. Standard, single-point Raman spectra were acquired at room temperature by employing a Renishaw inVia spectrometer, equipped with a 532 nm laser. The measurements were performed with a 50× objective, with a laser power of 0.1 mW, an integration time of 3 s, and 15 accumulations. Fiber-optic confocal Raman microscopy measurements were performed using a WITec alpha300 Apyron confocal microscope, fitted with a lens-based, 400 mm focal length ultrahigh throughput spectrometer (UHTS) and a Peltier-cooled back-illuminated deep depletion CCD camera for measurements in the near-infrared range (λ_{exc} 785 nm). All acquisitions were performed utilizing a 300 g mm^{-1} grid and a Zeiss semi-apochromatic, EC Epiplan-Neofluar 100× objective with a numerical aperture of 0.9, yielding an airy disk laser spot diameter of 1.064 μm for the 785 nm excitation line. Acquisition parameters were optimized to maximize the signal to noise (S/N) ratio while keeping the irradiance in the order of tens of thousands of W cm^{-2},[41] to avoid laser-induced MXene degradation: 1 s integration time, 5 accumulations, and a power of 0.5 mW at the objective, for an irradiance of 56.2 kW cm^{-2}. Mapping was performed over representative areas of the samples, ranging from a minimum of 10 × 12 μm^2 to a maximum of 30 × 30 μm^2, with a spatial resolution of 0.5 μm along both *x* and *y* directions. All generated spectra were treated for cosmic ray removal using the embedded filtering function in the WITec Project SIX Plus software; no baseline correction, background removal, or smoothing was performed. Raman images were generated from the acquired spectral maps by integrating each selected band using the peak maximum as the center and the baseline-defined width as the wavenumber

© 2026 The Author(s). Published by the Royal Society of Chemistry

limits. Spectral resolution for all measurements at λ_{exc} 785 nm is 1.91–1.36 cm^{-1} across the 100 to 2000 cm^{-1} range. X-ray photoelectron spectroscopy (XPS) spectra were acquired in an ultra-high-vacuum (UHV) chamber with a working pressure below 5×10^{-8} mbar, using the Al Kα line ($h\nu = 1486.7$ eV). Quantitative elemental analysis was carried out using sensitivity-factor-corrected peak areas extracted from the high-resolution spectra. Owing to the layered nature of the electrodes and the different information depths associated with the analysed core levels, elemental ratios were considered only as approximate estimates and were not used for rigorous stoichiometric analysis.

UV-vis diffuse reflectance spectra were recorded on the FTO substrate using a Jasco V-770 spectrophotometer, coupled with an integrating sphere. Band gap values were obtained from absorbance spectra using the Tauc plot equation:

$$(\alpha h\nu)^{1/n} = A(h\nu - E_g)$$

where α is the absorption coefficient, h is the Planck constant, ν is the frequency, E_g is the bandgap energy, and n is $\frac{1}{2}$ for direct band gap materials such as $BiVO_4$.[42]

2.4 Photoelectrochemical characterization

PEC measurements were conducted with an Autolab PGSTAT204 potentiostat and a Spectral Products ASB-XE-E180 xenon lamp light source, set to 100 mW cm^{-2} using an Oriel PV reference cell system. The substrate was irradiated with AM 1.5G light. The setup used was a three-electrode cell, employing an Ag/AgCl (saturated KCl) reference electrode, a platinum wire counter electrode, and a platinum clip as the working electrode. The electrolyte employed was Na_2SO_4 0.5 M with pH = 7. The samples were front illuminated through a quartz window on an Ossila glass PEC cell. Potentials referenced to the Ag/AgCl were converted to the RHE scale according to the following equation:

$$E\ (\text{V } \textit{vs.}\ \text{RHE}) = E\ (\text{V } \textit{vs.}\ \text{Ag/AgCl}) + 0.197\ \text{V} + 0.059\ \text{V} \times \text{pH}$$

LSV curves were acquired at a scan rate of 10 mV s^{-1}. EIS was conducted at 1.23 V, 1.4 V and 1.6 V *vs.* RHE under simulated solar light, in a range of frequencies from 100 kHz to 1 Hz. IPCE was calculated using 6 Thorlabs FKBV10 hard-coated Vis bandpass filters with wavelengths from 350 to 600 nm (10 nm fwhm) and the xenon lamp. The IPCE at a specific wavelength (λ) was obtained using the following formula:

$$\text{IPCE}\ (\%) = \frac{1240 \times I_{ph}}{\lambda \times J_{ph}} \times 100$$

where I_{ph} is the photocurrent density, λ is the incident wavelength and J_{ph} is the incident irradiance, measured thanks to an 843-R Newport optical power meter. Mott–Schottky measurements were performed using a BioLogic SP-150e potentiostat in the dark at 1 kHz. The donor density (N_d) was obtained from the slope $d(1/C_{SC}^2)/dV$, and the flat band potential can be obtained from the intercept of the linear fit with the X axis ($1/C_{SC}^2 = 0$), both using the formula:

$$N_d = \left(\frac{2}{A^2 e \varepsilon \varepsilon_0}\right)\left(\frac{1}{\mathrm{d}\dfrac{1}{\mathrm{d}\dfrac{C_{SC}^{\ 2}}{\mathrm{d}V}}}\right)$$

where A is the electrode area, e is the electron charge, ε is the dielectric constant for $BiVO_4$ (ref. 36 and 43) and ε_0 is the permittivity in a vacuum.

LSV curves with scavengers are measured in the aqueous electrolyte containing 0.5 M of Na_2SO_4 and 0.5 M of Na_2SO_3, and Na_2SO_3 acts as the hole scavenger. The charge transfer efficiency (η_{tr}) at 1.23 V *vs.* RHE is calculated using the following equation:

$$\eta_{tr}\ (\%) = \frac{J_{Na_2SO_4}}{J_{Na_2SO_4,Na_2SO_3}} \times 100$$

where $J_{Na_2SO_4}$ is the photocurrent density measured in 0.5 M of Na_2SO_4 and $J_{Na_2SO_4,Na_2SO_3}$ is the photocurrent density measured in an electrolyte containing Na_2SO_3.

Applied Bias Photon-to-Current Efficiency (ABPE) was calculated using the following equation:

$$\text{ABPE}\ (\%) = \frac{J \times (1.23 - V_{bias})}{P_{light}} \times 100$$

where J is the photocurrent density, V_{bias} is the applied potential *vs.* RHE (0.8V *vs.* RHE) and P_{light} is the light intensity (100 mW cm^{-2}).

IMPS data were obtained with an Ivium CompactStat potentiostat coupled with a LED ModuLight (Ivium). The measurements were acquired at 1.23 V *vs.* RHE in Na_2SO_4 0.5 M (pH = 7) with a white LED (P = 20 mW cm^{-2}). The light intensity was measured using a Si-photodiode positioned at the same location as the sample. The amplitude oscillation was set to 10% of the DC light intensity, with the modulation frequency ranging from 5 kHz to 0.2 Hz. The acquired data are displayed in the complex plot of the dimensionless transfer function defined as

$$Q = \frac{\tilde{J}}{\widetilde{J_\phi}}$$

where $\widetilde{J_\phi} = q\varphi$ is the modulated photon flux expressed as current density, with φ being the photon flux (s^{-1} cm^{-2}) at 550 nm (the maximum wavelength of the emission spectrum of the light) and q being the elementary charge. $\tilde{J}$ is the corresponding modulating photocurrent density (A cm^{-2}).

3 Results and discussion

3.1 Structural and morphological characterization

$BiVO_4$ and $BiVO_4/FePO_4$ electrodes were fabricated on fluorine-doped tin oxide (FTO) substrates using an Autodrop setup (see the Experimental section and Fig. 1 for details).[16] The optimized fabrication parameters for $BiVO_4$ and $BiVO_4/FePO_4$ photoanodes were selected based on our group's previous report. Subsequently, MXene layers were deposited onto the electrodes *via* an automated spray coating process using exfoliated MXene

© 2026 The Author(s). Published by the Royal Society of Chemistry

nanosheets prepared by the etching and delamination procedures described in the Experimental section. Two MXene loadings were tested by applying 100 and 150 automated spray coating cycles. Accordingly, the MXene-modified electrodes are denoted as $BiVO_4$ 100L, $BiVO_4$ 150L, $BiVO_4/FePO_4$ 100L, and $BiVO_4/FePO_4$ 150L, where "L" refers to the number of spray-coating layers. The structural properties were analysed with X-ray diffraction (XRD) (Fig. S2). All the samples exhibit identical diffraction features, which can be primarily assigned to the monoclinic scheelite phase of $BiVO_4$ (ICSD 100602).[44] No crystalline $FePO_4$ phases are detected, consistent with the amorphous nature of $FePO_4$ synthesized *via* the Autodrop process.[16] For $BiVO_4/FePO_4$ 150L, a broad diffraction peak centered at ~7.5° is observed and attributed to the (002) reflection of $Ti_3C_2T_x$. This peak is shifted from 9.8° in the Ti_3AlC_2 phase (ICSD 153266) due to the etching process, which removes the Al layers and increases the interlayer spacing of the titanium carbide structure. The enlarged interlayer distance, together with the broadening of the (002) peak, indicates the formation of highly exfoliated and ultrathin MXene layers.[45] No distinct diffraction peaks corresponding to MXene are observed for the $BiVO_4/FePO_4$ 100L sample, which is likely due to the low loading and ultrathin nature of the deposited MXene nanosheets. Nevertheless, the presence of MXene in all MXene-modified samples is further confirmed by the morphological analysis shown in Fig. 2. SEM combined with EDX analysis was employed to investigate surface morphology and elemental distribution. As shown in Fig. 2, all the samples exhibit a heterogeneous surface morphology dominated by fine granular particles characteristic of $BiVO_4$ (Fig. 2a and b) and $BiVO_4/FePO_4$ (Fig. 2c and d). The introduction of the thin $FePO_4$ layer does not noticeably alter the surface morphology of the electrode. With increasing MXene loading, the granular matrix becomes progressively covered by ultrathin MXene nanosheets, indicating a high degree of exfoliation. In samples coated with 150 spray-coating cycles (Fig. 2b and d), MXene flakes are more clearly visible compared to those with 100 layers (Fig. 2a and c). However, the surface coverage remains non-uniform, leaving partially exposed regions of the underlying $BiVO_4/FePO_4$ matrix. EDX elemental mapping (Fig. 2e–j) reveals the presence of V, Bi, Fe, P, and Ti, confirming the successful deposition of both $FePO_4$ and MXene layers on the $BiVO_4$ substrate. Notably, the spatial distribution of Ti closely matches the flake-like features observed in the SEM image, further verifying that the thin overlayer corresponds to $Ti_3C_2T_x$ MXene.

3.2 Surface characterization

Standard single-point Raman spectra of the samples are presented in Fig. S3. Using a conventional excitation wavelength for $BiVO_4$-based materials (λ_{exc} = 532 nm), all the samples display identical Raman features, regardless of their layered composition. These bands are characteristic of monoclinic scheelite-type $BiVO_4$.[37] The peaks at 326 and 366 cm^{-1} are assigned to the antisymmetric and symmetric bending modes of the tetrahedral VO_4^{3-} units, respectively. Additionally, a shoulder at 710 cm^{-1} and a prominent band at 827 cm^{-1} correspond to the antisymmetric and symmetric V–O stretching

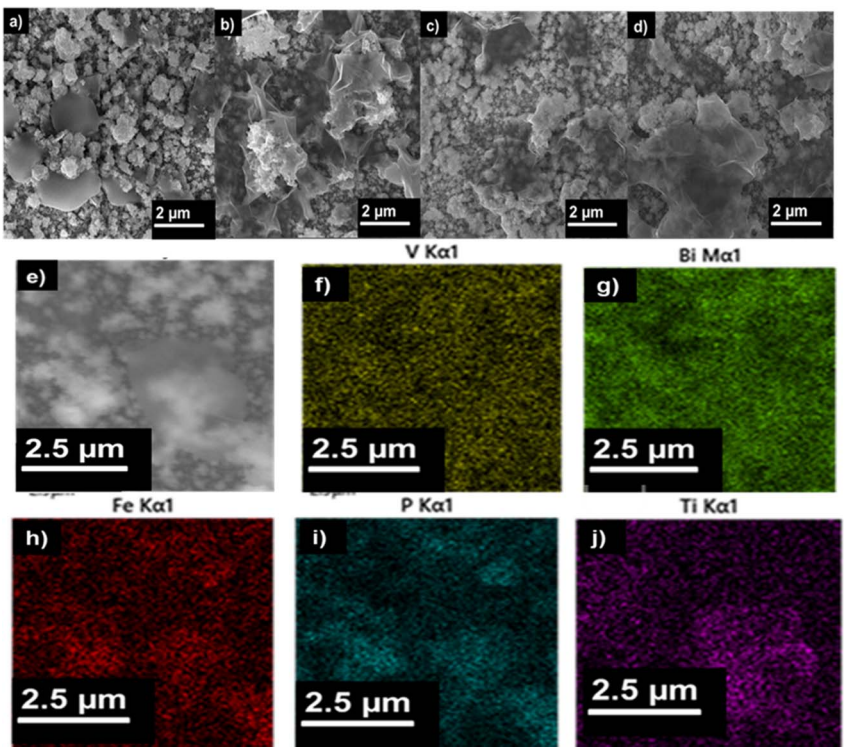

Fig. 2 SEM image of (a) $BiVO_4$ 100L; (b) $BiVO_4$ 150L; (c) $BiVO_4/FePO_4$ 100L; (d) $BiVO_4/FePO_4$ 150L; (e) SEM image; EDX maps of $BiVO_4/FePO_4$ 100L (f) EDX map of V; (g) EDX map of Bi; (h) EDX map of Fe; (i) EDX map of P; (j) EDX map of Ti.

© 2026 The Author(s). Published by the Royal Society of Chemistry

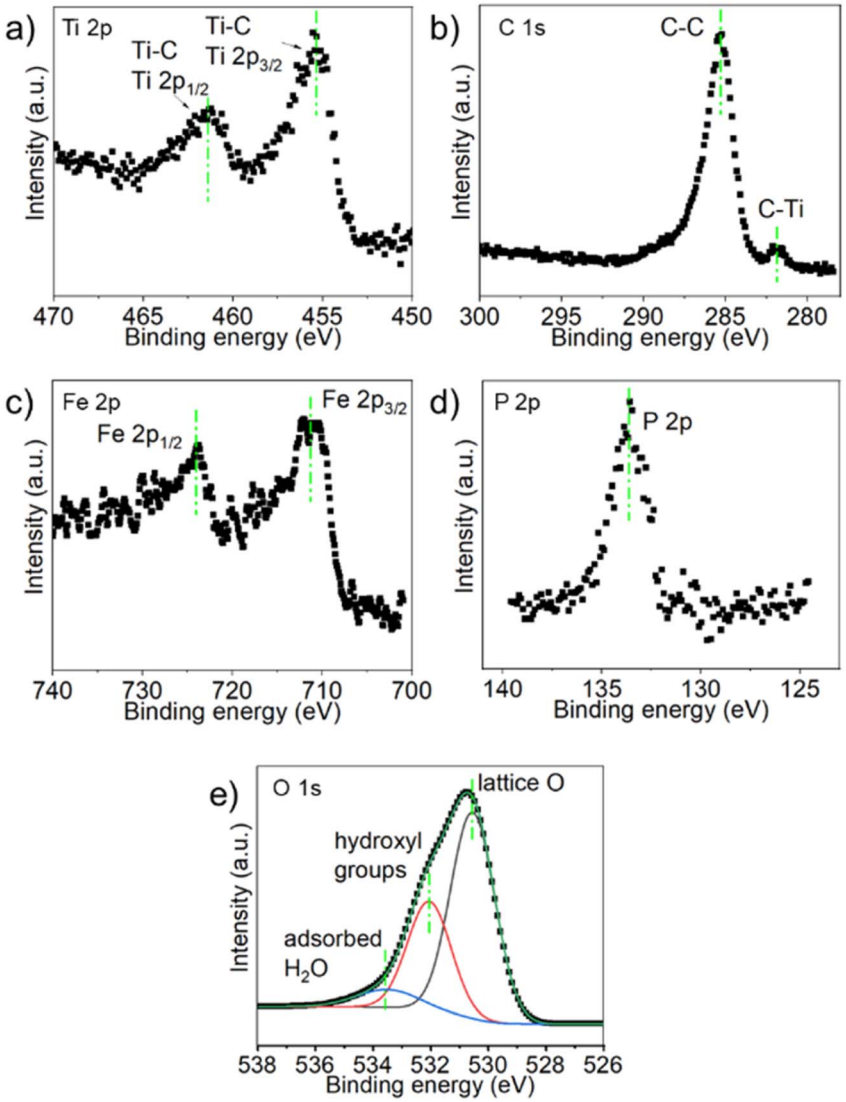

Fig. 3 High resolution XPS spectra of $BiVO_4/FePO_4$ 100L: (a) Ti 2p, (b) C 1s, (c) Fe 2p, (d) P 2p and (e) O 1s.

vibrations.[46] As expected under these measurement conditions, amorphous $FePO_4$ is not detected. Likewise, no distinct vibrational modes attributable to MXene are observed. These results can be reasonably explained by several factors: (i) the ultrathin nature of the MXene overlayer,[47] (ii) resonance enhancement of the $BiVO_4$ signal due to the excitation wavelength being close to its band gap (Fig. 4),[48] and (iii) the laser focusing configuration, which results in a penetration depth and focal volume that preferentially probe the underlying $BiVO_4$ rather than the superficial ultrathin MXene layers.

To directly assess the surface chemistry of the pristine $BiVO_4/FePO_4$/MXene photoanode, XPS analysis was performed on the representative $BiVO_4/FePO_4$ 100L sample. The survey spectrum shows no detectable Cl, F, Sn, Al, or Li signals, excluding significant residual chloride from $FeCl_3$ precursors, detectable residues from MXene etching/delamination processes, and measurable exposure of the underlying FTO substrate (Fig. S4). The Ti 2p and C 1s spectra provide evidence for the presence of Ti_3C_2-derived MXene on the electrode.[49] In particular, the Ti 2p region shows a low-binding-energy contribution at approximately 455.3 eV for Ti $2p_{3/2}$ and 461.4 eV for Ti $2P_{1/2}$, which are characteristic peaks of Ti–C bonding in titanium carbide/MXene environments. This assignment is further supported by the C 1s spectrum, where a carbide-related component is observed at approximately 282.0 eV. The simultaneous observation of these Ti–C and C–Ti contributions confirm the presence of TiC-like bonding associated with the MXene phase in the $BiVO_4/FePO_4$ 100L photoanode. Importantly, the preservation of these carbide-related features indicates that the deposition onto the underlying $BiVO_4/FePO_4$ layer does not substantially alter the intrinsic carbide chemistry of the MXene flakes. In addition, the Fe 2p and P 2p regions confirm the presence of Fe-containing phosphate species at the electrode surface. In particular, the Fe 2p line shape is consistent with the intended formation of an $FePO_4$ interfacial layer, in agreement with reference $FePO_4$ spectra reported in the

© 2026 The Author(s). Published by the Royal Society of Chemistry

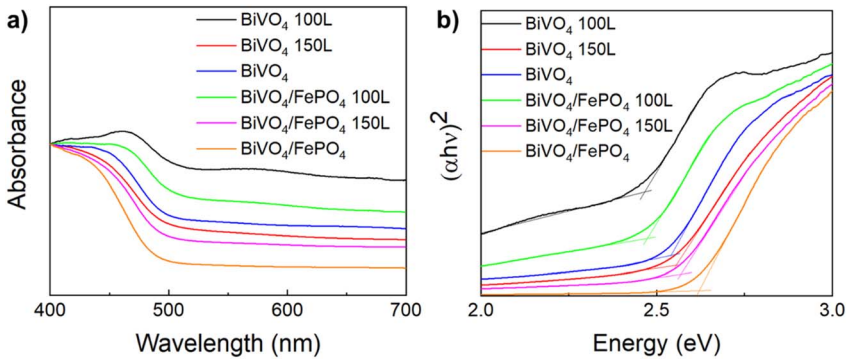

Fig. 4 (a) UV-vis absorption spectra and (b) Tauc plots of all the studied photoelectrodes.

literature.[50] The Bi 4f and V 2p signals are strongly attenuated, consistent with the presence of superficial $FePO_4$/MXene-derived overlayers within the XPS probing depth (Fig. S4). The O 1s spectrum can be deconvoluted into three main components associated with lattice oxygen (530.6 eV), hydroxyl groups (532.1 eV), and adsorbed water species (533.5 eV) (Fig. 3e).[51] The spectra are dominated by lattice oxygen and hydroxyl-related contributions, indicating no major restructuring of the oxide/phosphate surface.

3.3 Optical characterization and band gap analysis

UV-vis diffuse reflectance spectroscopy (DRS) equipped with an integrating sphere was employed to investigate the optical properties of the samples. The optical band gaps were determined from the UV-vis spectra using Tauc plots assuming a direct allowed transition (Fig. 4). Pristine $BiVO_4$ exhibits an absorption edge at approximately 490 nm, corresponding to a direct band gap of 2.54 eV, in good agreement with previous reports.[52] Upon modification with amorphous $FePO_4$ and MXene, the band gap values remain within a range of 2.45–2.60 eV, indicating that these surface modifications do not significantly alter the intrinsic electronic structure of $BiVO_4$. This observation confirms that $FePO_4$ and MXene are predominantly superficial layers and induce only subtle changes in the fundamental band structure. Nevertheless, slight variations among the samples can be observed. The absorption edge of $BiVO_4/FePO_4$ shows a minor blueshift accompanied by a small increase in the apparent band gap, suggesting limited electronic interaction between $BiVO_4$ and the amorphous $FePO_4$ overlayer.[53] Overall, the absorption spectra remain dominated by the characteristic $BiVO_4$ absorption edge in the visible region. In contrast, the introduction of thin MXene coatings (100 layers) results in a slight redshift of the absorption edge and a reduced apparent band gap, along with enhanced visible-light absorption and a broadened photoresponse region. This behavior is attributed to strong interfacial electronic coupling at the $BiVO_4$/MXene interface, which promotes charge-transfer-related optical transitions and introduces additional electronic states near the band edges.[35] Because the MXene layer remains thin and partially discontinuous at this loading, these interfacial effects are maximized without significantly obscuring the intrinsic absorption characteristics of $BiVO_4$, as supported by the SEM observations (Fig. 2). However, further increasing the MXene thickness to 150 spray coating layers does not lead to a continued decrease in the band gap. Instead, the apparent band gap shifts back toward that of pristine $BiVO_4$. This can be explained by the formation of thicker MXene overlayers, where upper MXene sheets partially screen the interfacial interaction between the underlying MXene layer and the $BiVO_4$ (or $BiVO_4/FePO_4$) surface. As a result, the electronic coupling becomes less effective, diminishing charge transfer contributions and allowing the intrinsic $BiVO_4$ optical response to dominate.[28]

3.4 Band edge assessment (Mott–Schottky plot)

Electrochemical impedance spectroscopy was employed to evaluate the flat-band potential (E_{fb}) and donor density (N_d) of the photoanodes. The Mott–Schottky plots (Fig. 5) show positive slopes for all samples, confirming their characteristic n-type behavior. The flat-band potential was determined by extrapolating the linear portion of the $1/C^2$ *versus* potential plot to the potential axis. Physically, E_{fb} corresponds to the applied potential at which band bending at the semiconductor/electrolyte interface disappears, meaning that the energy bands are flat and no space-charge region is present. As shown in Fig. 5, $BiVO_4/FePO_4$ 100L exhibits the most positive flat-band

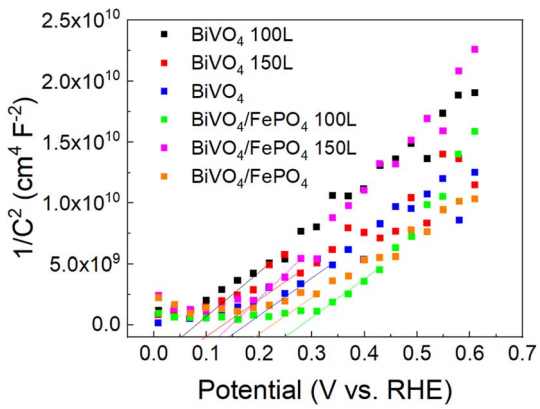

Fig. 5 Mott–Schottky plot of all the studied photoelectrodes.

© 2026 The Author(s). Published by the Royal Society of Chemistry

Table 1 Values of slope, E_{fb}, donor density N_d, energy of conductive band E_{CB}, energy of valence band E_{VB} (obtained from Mott–Schottky plots)[54] and band gap E_g (obtained from Tauc plots) of all the studied photoelectrodes

Sample	$BiVO_4$ 100L	$BiVO_4$ 150L	$BiVO_4$	$BiVO_4/FePO_4$ 100L	$BiVO_4/FePO_4$ 150L	$BiVO_4/FePO_4$
Slope	3.69×10^{10}	3.00×10^{10}	2.90×10^{10}	2.77×10^{10}	4.81×10^{10}	2.80×10^{10}
E_{fb} (V *vs.* RHE)	0.05	0.10	0.12	0.24	0.14	0.19
N_d (cm^{-3})	5.60×10^{17}	6.90×10^{17}	7.17×10^{17}	7.51×10^{17}	4.33×10^{17}	7.43×10^{17}
E_{CB} (V *vs.* RHE)	−0.02	0.03	0.05	0.17	0.06	0.12
E_{VB} (V *vs.* RHE)	2.45	2.58	2.59	2.64	2.63	2.74
E_g (eV)	2.47	2.55	2.54	2.47	2.57	2.62

potential (0.25 V *vs.* RHE) among all samples, indicating that the conduction band edge shifts toward more positive potentials. While the deposition of MXene alone does not significantly alter the position of E_{fb}, the introduction of the $FePO_4$ layer clearly shifts E_{fb} toward more positive values (Table 1), highlighting its influence on interfacial energetics. The slopes of the MXene-modified samples remain comparable to those of pristine $BiVO_4$ and $BiVO_4/FePO_4$, suggesting that MXene primarily affects surface energetics rather than substantially modifying the bulk carrier density.[16] The donor densities were calculated using the Mott–Schottky equation (see the Experimental section). The incorporation of MXene leads to a slight increase in donor density from 7.43×10^{17} cm^{-3} for $BiVO_4/FePO_4$ to 7.51×10^{17} cm^{-3} for $BiVO_4/FePO_4$ 100L, indicating a marginal enhancement in charge carrier concentration. However, excessive MXene loading (150 layers) results in a reduced donor density and a more negative flat-band potential (0.14 V *vs.* RHE for $BiVO_4/FePO_4$ 150L), which may be attributed to electronic shielding effects caused by the thicker MXene overlayer. Additionally, $FePO_4$ incorporation itself contributes to an increase in donor density, as $BiVO_4/FePO_4$ exhibits a higher N_d compared to pristine $BiVO_4$.

3.5 Photoelectrochemical characterization

3.5.1 PEC OER. The photoelectrochemical performances were assessed by studying the OER for all the prepared samples. All measurements were performed in 0.5 M Na_2SO_4 aqueous electrolyte (pH 7) under simulated AM 1.5G solar irradiation. The corresponding linear sweep voltammetry (LSV) curves are shown in Fig. 6. Negligible dark currents are observed for all photoanodes, indicating the absence of significant electrochemical reactions in the dark. The onset potential (at which a positive current is measured) for the PEC OER remains at approximately 0.45 V *vs.* RHE for all samples, suggesting that the fundamental reaction mechanism is not markedly altered by the surface modifications. Nevertheless, the photocurrent density is strongly influenced by the incorporation of $FePO_4$ and MXene. The introduction of the $FePO_4$ layer enhances the photocurrent compared to pristine $BiVO_4$, as evidenced by the higher current densities across the applied potential range. The beneficial effect of MXene is observed only when a thin layer (100 layers) is applied, as shown in Fig. 6a and d. In contrast, samples with thicker MXene coatings (150 layers) exhibit reduced photocurrent densities (Fig. 6b and e), indicating that excessive MXene loading negatively affects charge transport or increases recombination. The best performance is achieved by the $BiVO_4/FePO_4$ 100L photoanode, which delivers a photocurrent density of 2.3 mA cm^{-2} at 1.23 V *vs.* RHE. This value represents nearly a twofold enhancement compared to the $BiVO_4/FePO_4$ electrode without MXene (1.3 mA cm^{-2} at 1.23 V *vs.* RHE), highlighting the synergistic effect of optimized $FePO_4$ and MXene surface modification. The improved photoelectrochemical performance can therefore be attributed to a synergistic effect between the $FePO_4$ interlayer and the MXene overlayer. The $FePO_4$ layer likely facilitates hole transfer and passivates surface states of $BiVO_4$, while the highly conductive MXene nanosheets provide efficient pathways for electron extraction. Such complementary charge-transfer pathways help suppress interfacial recombination and promote directional charge transport across the photoanode–electrolyte interface. This cooperative interfacial design plays a key role in enhancing the PEC performance. A comparison with representative $BiVO_4$-based photoanodes reported in the literature is provided in Table S1.[4,17,55–57] Although the PEC performance reported here does not yet match the current state-of-the-art PEC performance, the significance of this work lies in demonstrating a scalable proof-of-concept for constructing $BiVO_4/FePO_4$/MXene heterostructured photoanodes using the combined Autodrop and automated dip-coating strategy. This fabrication approach provides a versatile platform for future optimization of both material composition and device performance.

The applied bias photon-to-current efficiency (ABPE), calculated from the LSV measurements, is shown in Fig. S5. The $BiVO_4/FePO_4$ 100L photoanode exhibits the highest ABPE values over the investigated potential range, reaching a maximum of approximately 0.43%, confirming the beneficial effect of the MXene modification on the overall PEC performance. Chronoamperometric measurements were conducted at 1.23 V *vs.* RHE under chopped illumination to provide a direct comparison of the photocurrent responses among the different samples (Fig. 7a). All the samples exhibit stable and reproducible photocurrent signals, and the overall trend is consistent with the LSV results, where the potential was linearly increased. The incorporation of $FePO_4$ enhances the photocurrent compared to pristine $BiVO_4$, and the introduction of a thin MXene overlayer ($BiVO_4$ 100L) improves the photoresponse as well. The combined modification with $FePO_4$ and an optimally thin MXene layer delivers the best performance, with $BiVO_4/FePO_4$ 100L achieving a steady-state photocurrent exceeding 2 mA cm^{-2}, approximately twice that of pristine $BiVO_4$ under

© 2026 The Author(s). Published by the Royal Society of Chemistry

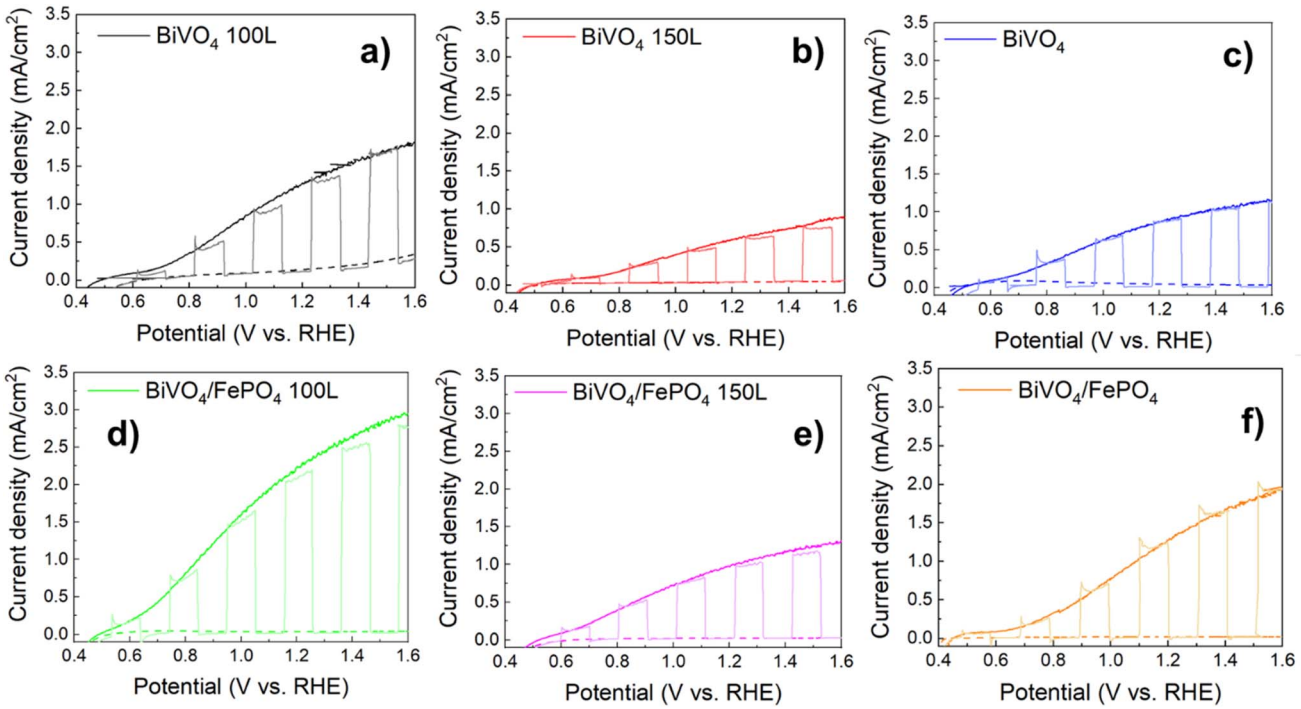

Fig. 6 LSV curves showing dark currents (dashed lines), light currents (thick solid lines) and chopped current (solid thin lines): (a) $BiVO_4$ 100L; (b) $BiVO_4$ 150L; (c) $BiVO_4$; (d) $BiVO_4/FePO_4$ 100L; (e) $BiVO_4/FePO_4$ 150L; (f) $BiVO_4/FePO_4$.

identical conditions. In contrast, a thicker MXene coating (150 layers) suppresses the photocurrent, as evidenced by the lower performance of both $BiVO_4$ 150L compared to $BiVO_4$ 100L and $BiVO_4/FePO_4$ 150L compared to $BiVO_4/FePO_4$ 100L. Moreover, the incident photon-to-current conversion efficiency (IPCE) of the $BiVO_4/FePO_4$ 100L photoanode demonstrates a substantial improvement in its overall photoresponse, reaching approximately 16.5% at 450 nm, compared with only ~8–9% for $BiVO_4/FePO_4$ and unmodified $BiVO_4$ at the same wavelength (Fig. S5). This remarkable enhancement is attributed to the synergistic interaction between the $FePO_4$ layer and the optimally thin $Ti_3C_2T_x$ MXene overlayer, which promotes more efficient charge separation, facilitates hole extraction, and accelerates interfacial charge transfer during photoelectrochemical water oxidation. Notably, all $FePO_4$-containing photoanodes display an anodic peak of the photocurrent immediately upon illumination, followed by a decay of the transient photocurrent to a steady-state value. This transient overshoot is correlated with the accumulation of photogenerated holes at the electrode surface, leading to enhanced surface recombination.[11] With the introduction of MXene, the accumulation of photogenerated holes at the surface is reduced, indicating that the MXene overlayer facilitates hole transfer and suppresses surface charge recombination. It is important to note that $FePO_4$ does not contribute significantly to light absorption and therefore does not directly enhance the IPCE response. Instead, its role is primarily interfacial: amorphous $FePO_4$ acts as a hole-accepting layer and redox mediator. In particular, Fe^{3+} species can be oxidized to Fe^{4+} intermediates under operation, which are widely reported as active centers for water oxidation, facilitating O–O bond formation and improving surface reaction kinetics.[58,59] In parallel, the phosphate matrix contributes to surface passivation and enhanced charge transfer by stabilizing the $BiVO_4$ interface and suppressing recombination. This dual function explains the observed increase in photocurrent density despite minimal changes in optical properties.[16]

To further verify the role of surface hole accumulation, a hole sacrificial agent was added in the electrolyte to easily collect the surface holes from the depleted region in the photoanode (Na_2SO_3). As shown in Fig. 7b, the addition of sulphite induces a cathodic shift in the photocurrent onset for all samples, indicating the earlier initiation of sulphite oxidation compared to water oxidation. Under these conditions, the photocurrent density of $BiVO_4/FePO_4$ 100L increases significantly to 5.32 mA cm^{-2}, approximately 2.3 times higher than that measured in Na_2SO_4 alone, confirming that surface recombination substantially limits the water oxidation performance. Furthermore, the LSV curves in both pure Na_2SO_4 and Na_2SO_3-containing electrolytes reveal that $BiVO_4/FePO_4$ 100L exhibits a noticeably steeper slope than pristine $BiVO_4$ and $BiVO_4/FePO_4$, demonstrating accelerated surface oxidation kinetics. Collectively, the transient photocurrent and LSV analyses indicate that the synergistic modification with $FePO_4$ and MXene not only enhances surface reaction kinetics but also improves charge carrier density and bulk charge separation, leading to a pronounced enhancement in overall PEC performance. Charge transfer efficiency (η_{tr}) was calculated at 1.23 V *vs.* RHE to elucidate the specific roles of each component within the heterostructure. Pristine $BiVO_4$ exhibits an η_{tr} of 23%,

© 2026 The Author(s). Published by the Royal Society of Chemistry

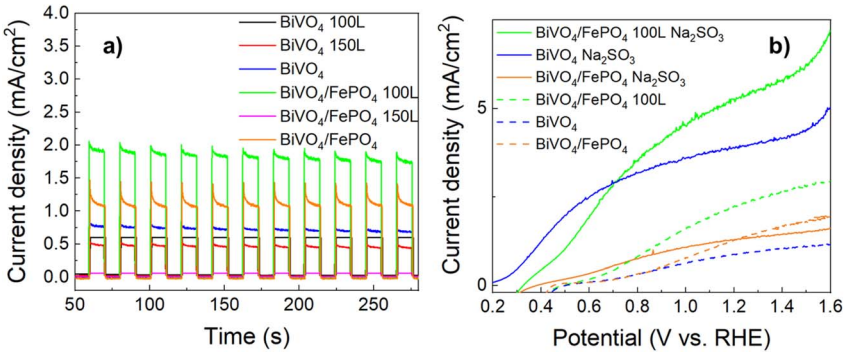

Fig. 7 (a) Chronoamperometry of all examined photoanodes at 1.23 V *vs.* RHE; (b) LSV curves showing dark currents (dashed lines) and light currents (thick solid lines) of samples $BiVO_4$, $BiVO_4/FePO_4$ and $BiVO_4/FePO_4$ 100L after adding Na_2SO_3 as a hole sacrificial agent in the neutral electrolyte.

indicating moderate interfacial hole transfer efficiency. Upon introducing only the $FePO_4$ layer, η_{tr} decreases to nearly zero, suggesting that although $FePO_4$ effectively passivates surface states and enhances bulk charge separation, it does not sufficiently promote interfacial water oxidation kinetics. As a result, surface hole transfer to water remains limited. In contrast, the incorporation of an optimized MXene overlayer dramatically increases η_{tr} to 43%, reflecting significantly improved interfacial hole transfer efficiency. This enhancement indicates that MXene provides an efficient conductive pathway and active interfacial platform for hole extraction, thereby increasing the charge transfer rate constant while suppressing surface recombination. Overall, the combined $FePO_4$/MXene modification produces a synergistic effect by coupling improved bulk charge separation (*via* $FePO_4$ passivation) with accelerated surface reaction kinetics (*via* MXene-mediated charge transfer), leading to substantially enhanced PEC performance.

3.5.2 EIS & IMPS. For a further investigation of the various charge phenomena of the photoelectrodes, photoelectrochemical impedance spectroscopy (PEIS) was employed at 1.23 V *vs.* RHE (Fig. 8a). As for the influence of MXene, the semicircle of Nyquist plots of the photoanode with thin MXene layers is comparable to that of the reference samples and much smaller than that of the electrodes with thick MXene layers, suggesting that thin MXene effectively reduces the impedance for charge transfer at the electrode–electrolyte interface, while thick MXene increases the resistance thus inhibiting the charge transfer. As for $FePO_4$, it contributes to decreasing the impedance as the semicircle of Nyquist plots of EIS of $BiVO_4/FePO_4$ is smaller than that of $BiVO_4$. The $BiVO_4/FePO_4$ 100L sample has the lowest charge transfer resistance R_{ct}, indicating an improvement in interfacial conductivity under the synergetic effect of $FePO_4$ and MXene (see details in Table S2). This trend resonates with the PEC properties of the samples. To quantify these interfacial charge transfer properties, the EIS spectra are fitted with the equivalent circuit shown in the inset of Fig. 8a. The R_{ct} was reduced from 5917 Ω to 3811 Ω after the modification of $BiVO_4$ with $FePO_4$ and MXene. Additionally, comparing dark *vs.* light measurements (Fig. S7), it can be confirmed that, upon light exposure, electron–hole pairs are formed and delivered to the photoelectrode/electrolyte interface, where they promote the OER and consequently lower the overall internal resistance, compared to dark conditions. The improved charge-transfer properties are consistent with the enhanced photocurrent observed in the LSV measurements.

To further elucidate the charge-transfer processes at the photoanode/electrolyte interface and the dynamics of photogenerated carriers, intensity-modulated photocurrent spectroscopy (IMPS) measurements were performed. IMPS probes the photocurrent response to small sinusoidal perturbations in light intensity at a fixed applied potential, with modulation frequencies ranging from 5 kHz to 0.2 Hz. Fig. 8b presents the IMPS spectra of the representative samples recorded at 1.23 V *vs.* RHE. Pristine $BiVO_4$, $BiVO_4/FePO_4$, and $BiVO_4/FePO_4$ 100L exhibit well-defined high-frequency semicircles in the fourth quadrant with clear intercepts on the real axis. Notably, the high-frequency intercept of $BiVO_4/FePO_4$ 100L shifts to higher values compared to the other samples, indicating an increased flux of photogenerated holes reaching the semiconductor/electrolyte interface. This observation is consistent with the enhanced PEC performance and the reduced charge-transfer resistance revealed by EIS measurements. At lower frequencies, a semicircle appearing in the first quadrant is typically associated with interfacial processes involving surface charge transfer and recombination.[60–62] Such features arise when the hole transfer rate is comparable to the recombination rate, reflecting limited charge separation efficiency. The progressive reduction or disappearance of this low-frequency semicircle is commonly observed in systems with optimized interfacial catalysts, at higher applied potentials where charge separation improves, or in the presence of hole scavengers that accelerate hole transfer. In the present study, all three samples display similar low-frequency behavior, with only a slightly more pronounced first-quadrant semicircle for pristine $BiVO_4$, suggesting stronger surface recombination and/or slower interfacial hole transfer compared to the $FePO_4$- and MXene-modified electrodes. When the frequency range is extended to lower values, $BiVO_4/FePO_4$ and $BiVO_4/FePO_4$ 100L exhibit a progressively flattened response rather than forming a fully closed semicircle (Fig. S8). This behavior may be qualitatively

© 2026 The Author(s). Published by the Royal Society of Chemistry

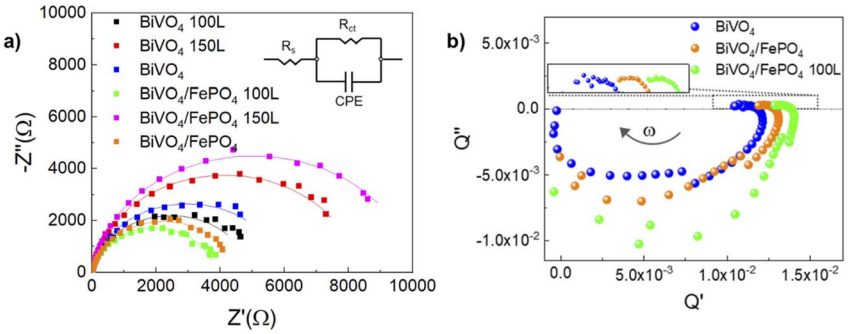

Fig. 8 (a) PEIS Nyquist plots at 1.23 V *vs.* RHE. Points are measured data while continuous lines are the Z-fit; (b) IMPS spectra measured in Na_2SO_4 0.5 M at 1.23 V *vs.* RHE. The inset shows the magnification of the low-frequency region located in the first quadrant of the complex plot. Data of samples $BiVO_4/FePO_4$ and $BiVO_4/FePO_4$ 100L are shown down to 1 Hz, while $BiVO_4$ data are shown down to 0.2 Hz.

attributed to the distribution of charge-transfer and recombination processes occurring on comparable time scales, without dominance of a single kinetic pathway. Such a distribution likely reflects spatial inhomogeneities in the $FePO_4$ and MXene coverage, in agreement with the non-uniform surface composition observed in the SEM–EDX maps (Fig. 2). Overall, the IMPS analysis indicates that the enhanced photocurrent in $BiVO_4/FePO_4$ and $BiVO_4/FePO_4$ 100L photoanodes primarily originates from improved carrier transport and reduced recombination losses prior to hole arrival at the electrolyte interface. The $FePO_4$ and MXene layers initially act as surface passivation layers that increase the effective hole flux at the interface. Their deposition moderately enhances interfacial kinetics by facilitating hole transfer; however, further improvement in coating uniformity may help suppress surface recombination more effectively by minimizing the distribution of interfacial surface states.

3.5.3 Stability test. A stability test of $BiVO_4/FePO_4$ 100L was conducted at 1.23 V *vs.* RHE at a light intensity of 100 mW cm^{-2} (Fig. 9a). After approximately 2 hours, the photocurrent retained about 70% of its initial value, indicating stability comparable to previously published work. Then $BiVO_4/FePO_4$ 100L after the stability test was examined to determine whether any noticeable changes had occurred. Morphological analysis revealed no significant variations. The post-reaction SEM image (Fig. 9b) shows that the $BiVO_4/FePO_4$ 100L retains the same characteristics observed prior to PEC testing (Fig. 2c). The MXene flakes remain clearly visible on the surface of $BiVO_4/FePO_4$ 100L. The cross-sectional SEM images revealed no significant morphological differences before and after the PEC measurements (Fig. S9). Furthermore, post-PEC XRD analysis (Fig. S10) showed diffraction peaks identical to those observed prior to the PEC measurements, indicating that the crystalline structure of the material remained unchanged. Then surface-sensitive characterization techniques including Raman spectroscopy and XPS were employed to investigate the surface changes of the photoanodes after PEC operation. The preserved presence and optical signature of MXene flakes on the surface of $BiVO_4/FePO_4$ 100L were further investigated by fiber-optic confocal Raman microscopy. Measurements were carried out under high magnification and at a high numerical aperture (100×, NA = 0.9) using a 785 nm excitation wavelength, deliberately chosen to be off-resonance with the band gap of the dominant $BiVO_4$ component while remaining close to an interband transition of $Ti_3C_2T_x$ MXene.[63] This strictly confocal configuration enhances the optical contribution from MXene flakes while minimizing the $BiVO_4$ background. A Raman mapping approach was adopted to account for the superficial inhomogeneity of the MXene coating. As shown in Fig. S11, under white-light illumination, the $BiVO_4/FePO_4$ 100L sample exhibits greater visual heterogeneity than the MXene-free $BiVO_4/FePO_4$ film, displaying patchy darker regions superimposed on the characteristic yellow crystalline $BiVO_4$ background. Raman imaging of the region indicated in Fig. 9c reveals that spectra collected from the darker areas (pink spectrum in Fig. 9g) differ markedly from those of the yellow regions (green spectrum in Fig. 9g). Within the spectral window between the VO_4^{3-} bending doublet (326 and 366 cm^{-1}) and the symmetric V–O stretching mode (~829 cm^{-1}), additional broad features appear that are consistent with $Ti_3C_2T_x$ MXene vibrational modes.[64–66] In particular, the darker areas exhibit (i) a sharp, resonant in-plane skeletal mode at ~120 cm^{-1}, (ii) a broad low-intensity band in the 260–280 cm^{-1} range associated with in-plane vibrations of F- and HO-terminated surface groups, (iii) a broad but more pronounced contribution at around 360–370 cm^{-1} attributed to in-plane modes of surface terminations, (iv) a band at ~510 cm^{-1} corresponding to the resonant ω_6 out-of-plane breathing mode of surface groups, (v) a broad feature centered approximately at ~570, ~620, and ~670 cm^{-1} assigned to in-plane carbon lattice vibrations influenced by different degrees of oxidation of the surface groups, and (vi) a relatively sharper band at ~727–730 cm^{-1} assigned to the resonant out-of-plane ω_3 mode of carbon atoms, consistent with the flake-like nature and synthesis route of the 2D material.[41,66,67] Importantly, characteristic $BiVO_4$ modes remain visible in these MXene-enriched regions, including the symmetric V–O stretch at ~829 cm^{-1} and the external lattice mode at ~210 cm^{-1}, with the latter exhibiting a slight asymmetry due to an MXene-related shoulder near 190 cm^{-1} attributed to out-of-plane skeletal vibrations.[41,46,66] The persistence of $BiVO_4$ features confirms the ultrathin nature of the MXene flakes, whose limited thickness prevents complete optical isolation of the layered contributions even under confocal

© 2026 The Author(s). Published by the Royal Society of Chemistry

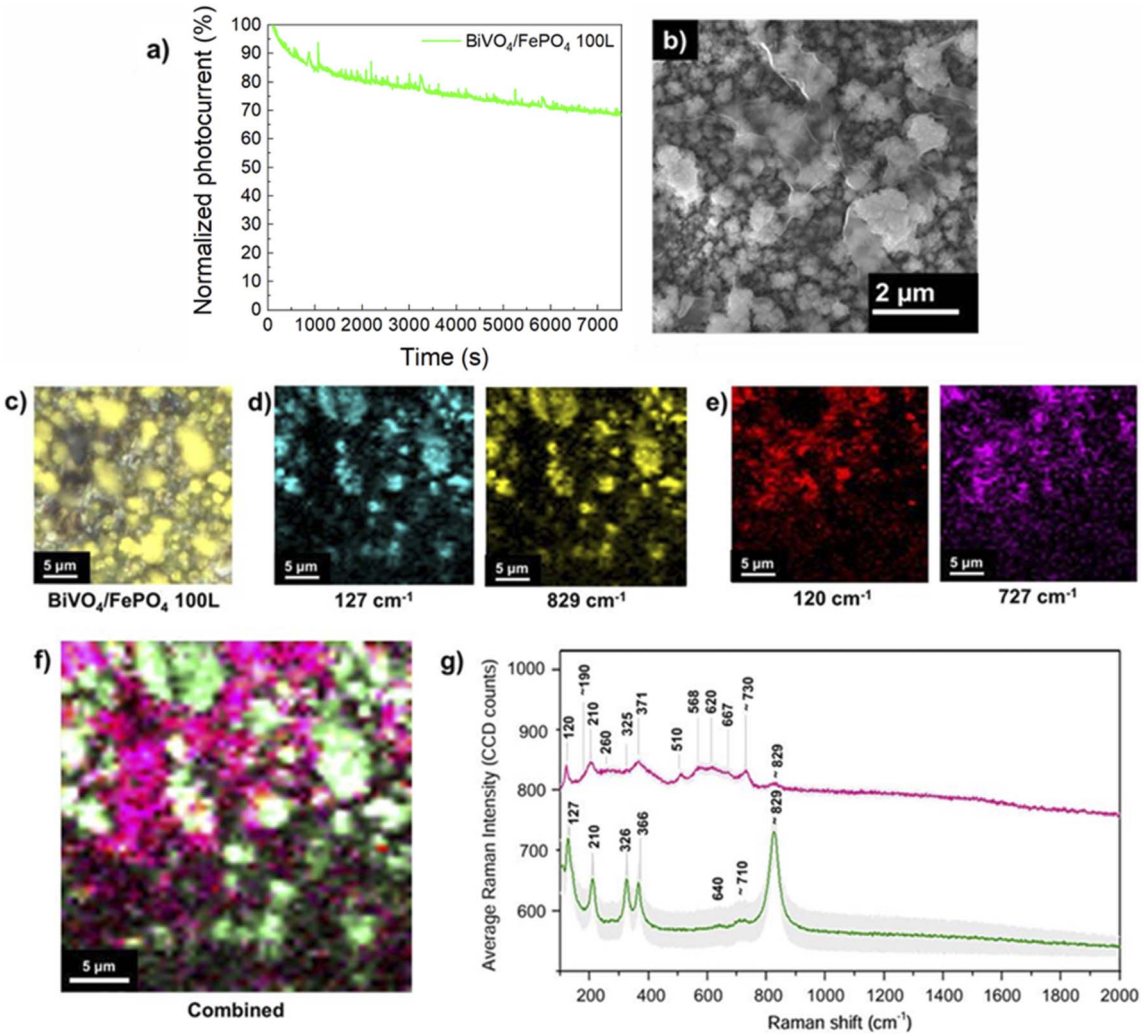

Fig. 9 (a) Stability test on $BiVO_4/FePO_4$ 100L performed under illumination at 1.23 V *vs.* RHE; (b) SEM image of $BiVO_4/FePO_4$ 100L post PEC; (c)–(g) Raman imaging (λ_{exc} 785 nm) of a representative area of the $BiVO_4/FePO_4$ 100L sample after PEC measurements. (c) White light optical microscopy image of the mapped area. (d) Spatial distribution of the integrated Raman intensities centered at 127 cm^{-1} and 829 cm^{-1} which are utilized as the $BiVO_4$ marker bands. (e) Spatial distribution of the integrated Raman intensities centered at 120 cm^{-1} and 727 cm^{-1} which are assigned to $Ti_3C_2T_x$ MXene; (f) combined 127 + 829 + 120 + 733 cm^{-1} channels, highlighting the spatial correlation between the 127 and 829 cm^{-1} bands with the predominantly yellow areas ($BiVO_4$), and the 120 + 733 cm^{-1} bands with the darker areas ($Ti_3C_2T_x$ MXene) in the white light optical microscopy image (panel c); (g) average Raman spectra of the two components that emerge from the combined channel map in panel f. The top, pink spectrum is characterized by the MXene signature with residual $BiVO_4$ contributions, while the bottom, green spectrum displays $BiVO_4$ features only. Shadowed gray bands represent the standard deviation of the mean Raman intensity. Spectra are vertically offset for clarity.

conditions. In contrast, the yellow regions dominated by the $BiVO_4$ Raman profile display only a minor broad contribution at ~640 cm^{-1}, attributable to the symmetric stretching of shorter V–O bonds within the vanadate tetrahedra and observed in the pristine $BiVO_4/FePO_4$ sample,[68] thereby excluding contributions from titanium carbide in those areas. As expected, amorphous $FePO_4$ is undetectable under these experimental conditions. For comparison, the MXene-free $BiVO_4/FePO_4$ sample exhibits the typical appearance of $BiVO_4$ films, characterized by yellow crystals on a black, yet $BiVO_4$-containing, background, as shown in Fig. S12 and S13. All the areas including dark and yellow regions show exclusively the characteristic vibrational modes of $BiVO_4$, with no additional spectral features detected.

Spatial mapping of the characteristic MXene bands at ~120 and ~727 cm^{-1} across the 100L sample is presented in Fig. 9d, while the $BiVO_4$-related modes at 127 and 829 cm^{-1} recorded over the same region are shown in Fig. 9e. The MXene-associated signals exhibit higher intensity within the darker areas identified in Fig. 9c, whereas the $BiVO_4$ characteristic peaks are more pronounced in the yellow regions. A combination color map incorporating all the bands displayed in Fig. 9d and e is provided in Fig. 8f. This map reveals a coherent spatial distribution that closely follows the darker regions observed under white-light illumination (Fig. 9c) and mirrors the patchy flake morphology observed by SEM (Fig. 2c), thereby confirming the persistent presence of 2D $Ti_3C_2T_x$ MXene on the surface of

© 2026 The Author(s). Published by the Royal Society of Chemistry

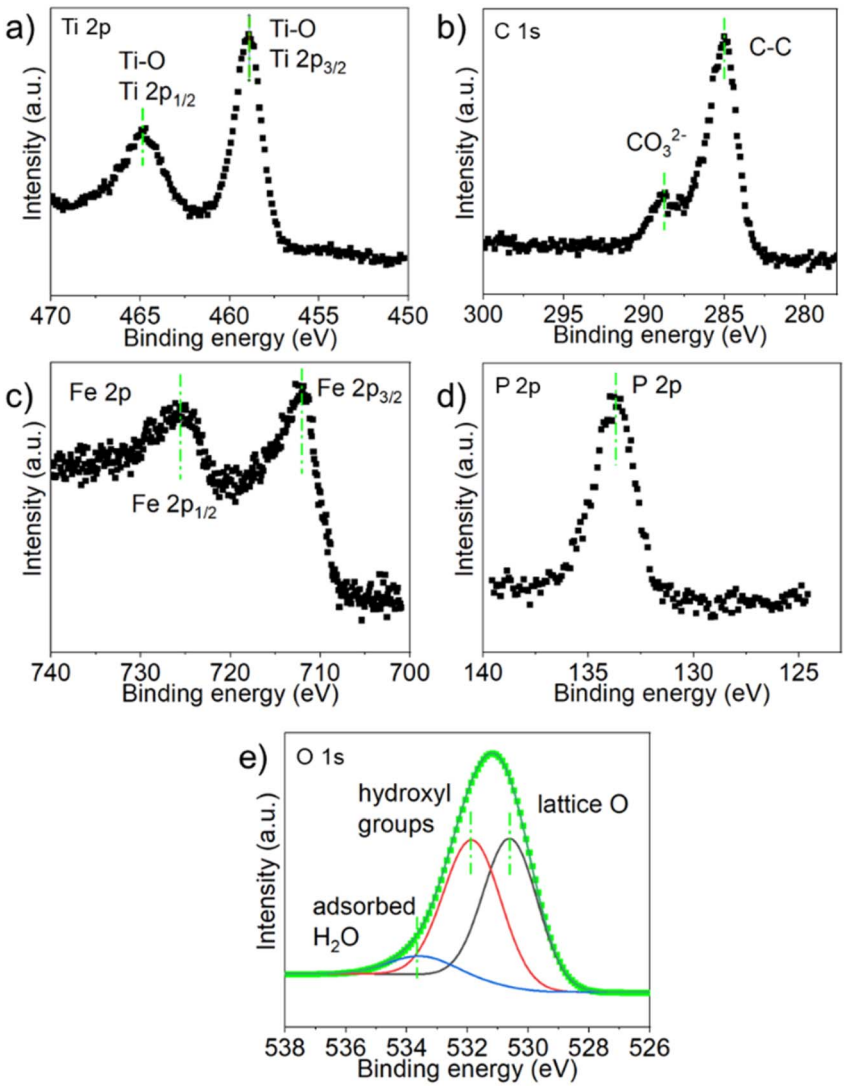

Fig. 10 High resolution XPS spectra of $BiVO_4/FePO_4$ 100L after the stability test: (a) Ti 2p, (b) C 1s, (c) Fe 2p, (d) P 2p and (e) O 1s.

the $BiVO_4/FePO_4$ 100L sample after PEC operation. Importantly, no additional spectral features indicative of electrochemical oxidation or photothermal degradation are detected. In particular, there is no evidence of TiO_2 formation (typically appearing at 140–150 cm^{-1}) nor of graphitic or amorphous carbon species, which would be characterized by prominent D and G bands at approximately 1390 and 1580–1600 cm^{-1}, respectively. These findings, together with the preservation of the characteristic $Ti_3C_2T_x$ MXene vibrational signatures consistent with its original structure, demonstrate that both the $BiVO_4$ substrate and the MXene overlayer retain their structural integrity after 2 h of PEC OER operation.

Fig. 10 shows XPS analysis of the $BiVO_4/FePO_4$ 100L photoanode after the PEC stability test. As shown in Fig. 10a, the Ti–C carbide contribution is no longer clearly resolved after PEC testing, while the Ti 2p spectrum becomes dominated by higher-binding-energy Ti species centered at *ca.* 459.0 eV, consistent with TiO_x/TiO_2-like environments. Consistently, the carbide-related C–Ti component at *ca.* 282.0 eV in the C 1s spectrum disappears after PEC operation, while a weak contribution emerges at *ca.* 288.8 eV, attributable to carbonate species likely originating from electrolyte-related surface residues (Fig. 10b). These results indicate that the outermost MXene-derived surface undergoes substantial oxidation/reconstruction under PEC operating conditions. It is worth mentioning that the apparent discrepancy between XPS and Raman results can be rationalized by considering the different probing depths and sampling volumes of the two techniques. XPS is highly surface-sensitive and probes only the outermost few manometers of the electrode, approximately 6 nm under our experimental conditions. Therefore, the disappearance of the Ti–C/C–Ti components and the dominance of TiO_x/TiO_2-like signals after PEC testing indicate oxidation/reconstruction of the external surface of the MXene-derived flakes. In contrast, Raman microscopy probes a larger optical volume and remains sensitive to underlying, laterally exposed or partially oxidized MXene-derived domains, which explains the persistence of MXene-related vibrational features in Fig. 9d–f. These

© 2026 The Author(s). Published by the Royal Society of Chemistry

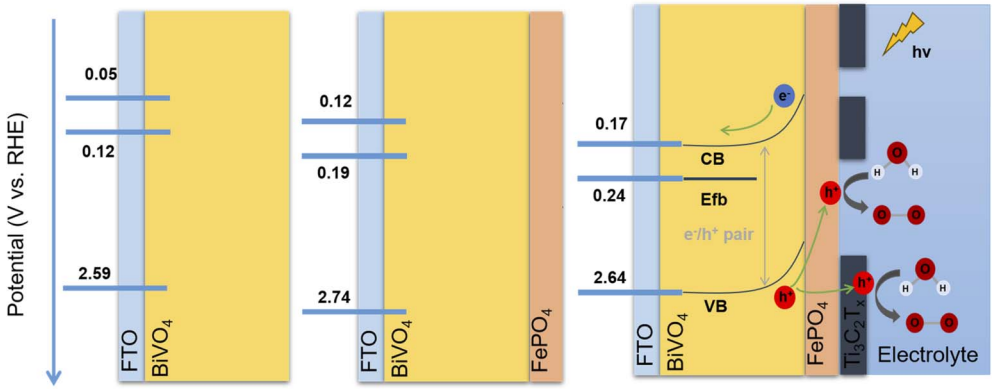

Fig. 11 Scheme for the proposed PEC water oxidation mechanism for the optimized $BiVO_4/FePO_4$/MXene photoanode.

observations indicate that PEC operation does not completely remove the MXene-derived overlayer, but induces oxidation of its outermost surface. This surface oxidation is likely one of the causes of the photocurrent decay observed during the 2 h stability test, as the formation of a TiO_x/TiO_2-like external layer may partially hinder the interfacial charge-transfer function originally provided by the MXene flakes. The Fe 2p and P 2p spectra retain the characteristic features observed before PEC testing, indicating that the $FePO_4$ layer is chemically preserved during operation (Fig. 10c and d). Due to the overlap between lattice oxygen, phosphate oxygen, hydroxylated species, adsorbed water and electrolyte-related residues, the O 1s region is used only as complementary evidence (Fig. 10e). Moreover, the quantitative XPS analysis (Table S3) indicates a decrease in the relative surface Ti contribution together with corresponding increases in the relative Bi, V, Fe and P contributions after the PEC stability test. Although these values should not be interpreted as rigorous stoichiometric quantities, they are consistent with partial oxidation and surface reconstruction of the MXene-derived overlayer, resulting in greater XPS sensitivity to the underlying $BiVO_4/FePO_4$ layers. This surface reconstruction is likely to contribute to the gradual photocurrent decay observed during the 2 h stability test.

3.6 Mechanism study

Based on the above results and analysis, the proposed PEC water oxidation mechanism for the $BiVO_4/FePO_4$/MXene photoanode is illustrated in Fig. 11. The system consists of a surface composite/overlayer configuration, where crystalline $BiVO_4$ is sequentially coated with an amorphous $FePO_4$ overlayer and a $Ti_3C_2T_x$ MXene surface layer, forming well-defined interfaces for charge transfer. As an n-type semiconductor, $BiVO_4$ possesses a flat band potential located close to its conduction band (Table 1). Upon modification with $FePO_4$ and MXene, the E_{fb} shifts progressively toward more positive values, from 0.12 V *vs.* RHE for pristine $BiVO_4$ to 0.19 V *vs.* RHE for $BiVO_4/FePO_4$ and further to 0.24 V *vs.* RHE for $BiVO_4/FePO_4$ 100L, while it shifts back to more negative values (0.14 V *vs.* RHE) for $BiVO_4/FePO_4$ 150L (Table 1 and Fig. 11). This anodic shift reflects a downward movement of modified interfacial energetics, resulting in adjusted band alignment and enhanced band bending at the semiconductor/electrolyte interface. Under illumination, photogenerated electrons in the conduction band of $BiVO_4$ are driven by the internal electric field toward the back contact and subsequently participate in the hydrogen evolution reaction at the cathode. Simultaneously, E_{fb} equilibration between the $BiVO_4/FePO_4$/MXene photoanode and the electrolyte establishes interfacial band bending that promotes directional electron transport toward the cathode and facilitates charge separation. Meanwhile, the valence band edge shifts slightly toward more negative potentials (from 2.74 V *vs.* RHE for $BiVO_4/FePO_4$ to 2.64 V *vs.* RHE for $BiVO_4/FePO_4$ 100L), consistent with the small reduction in the optical band gap after surface modification. The photogenerated holes in the valence band of $BiVO_4$ are efficiently transferred across the interfaces first to the $FePO_4$ layer and subsequently to the $Ti_3C_2T_x$ MXene overlayer, where water oxidation occurs. Together with the applied electric field, this stepwise hole extraction pathway suppresses surface recombination and promotes efficient hole utilization for the OER. Within this heterostructure, $FePO_4$ and $Ti_3C_2T_x$ MXene act as effective hole-accepting and transport layers. MXene enhances interfacial conductivity, accelerates charge transfer, and provides additional active sites for the OER, while $FePO_4$ functions both as a hole reservoir for passivation and as a cocatalyst, with Fe^{3+} species serving as catalytically active centers.[16,17] In addition, MXene slightly improves light harvesting and broadens the photoresponse range, as evidenced by the LSV results (Fig. 6) and UV-vis spectra (Fig. 4). Moreover, an optimally thin MXene overlayer maintains adequate exposure of the underlying $FePO_4$ surface, enabling balanced interfacial charge transfer between $FePO_4$ and MXene and thereby optimizing their synergistic contribution to the PEC OER. In contrast, excessive MXene loading reduces light absorption, partially shields the $FePO_4$ and $BiVO_4$ layers, weakens interfacial coupling, and ultimately diminishes the overall PEC performance.

4 Conclusions

In this work, heterostructured photoanodes for the OER were fabricated based on $BiVO_4$ and $BiVO_4/FePO_4$ prepared *via* the Autodrop method, followed by the deposition of $Ti_3C_2T_x$ MXene

© 2026 The Author(s). Published by the Royal Society of Chemistry

layers with controlled thickness using an automated spray coating technique. Comprehensive PEC characterization demonstrates that the synergistic integration of $FePO_4$ and MXene significantly enhances water oxidation performance. Among the investigated samples, the $BiVO_4/FePO_4$ 100L electrode exhibits the highest photocurrent density. The photoanode retains approximately 70% of its initial photocurrent after 2 h of PEC OER operation, demonstrating moderate operational stability. However, XPS analysis reveals partial oxidation of the MXene overlayer, indicating that additional strategies aimed at stabilizing the MXene surface or controlling its oxidation could further enhance the long-term durability of the photoanode. Mechanistic analysis reveals that both $FePO_4$ and MXene promote efficient charge separation: photogenerated electrons are effectively driven toward the cathode, while holes are extracted and transferred to the surface to participate in the OER. An optimized, ultrathin MXene overlayer ensures sufficient exposure of the underlying $FePO_4$, where Fe^{3+} species act as active co-catalytic sites for the OER. The enhanced performance is attributed to the combined effect of the $FePO_4$ interlayer and the MXene overlayer, which provide complementary functions in the photoanode architecture. While the $FePO_4$ layer improves the interfacial properties of $BiVO_4$ and facilitates hole transport, the conductive MXene nanosheets promote more efficient interfacial hole transfer between the electrode/electrolyte. In contrast, excessive MXene loading partially shields the active interface and limits performance.

Overall, these findings establish using $FePO_4$ and MXene overlayers as an effective strategy to boost the performance of $BiVO_4$-based photoanodes and suggest that future efforts should focus on fine-tuning MXene thickness and composition, as well as extending this automated approach to scalable production for solar fuel devices. The enhanced performance can be attributed to the complementary roles of the $FePO_4$ interlayer and the MXene overlayer, which together facilitate efficient charge separation and interfacial charge transfer. The use of Autodrop and automated spray deposition provides a practical route toward reproducible fabrication of MXene-modified photoelectrodes. These findings highlight the potential of combining conductive MXene nanosheets with catalytic interlayers as a versatile strategy for improving interfacial charge transport in semiconductor photoanodes and advancing scalable solar fuel technologies.

Conflicts of interest

There are no conflicts to declare.

Data availability

Additional datasets supporting this work have been included as part of the supplementary information (SI). The datasets generated and analyzed during this work can be made available from the authors on request.

Supplementary information (SI) is available. See DOI: https://doi.org/10.1039/d6na00469e.

Acknowledgements

This work was supported by the European Research Council through the project JANUS BI (ID: 101041229). C. D., L. F., and the fiber-optic confocal Raman analysis portion of this project have received funding from the European Research Council under the European Union's Horizon 2020 research and innovation programme (grant agreement no. 865819). I. P. and P. R. acknowledge that this work is part of the "Technologies for Sustainability" Flagship program of the Istituto Italiano di Tecnologia (IIT).

References

1 J. Joy, J. Mathew and S. C. George, Nanomaterials for photoelectrochemical water splitting – review, *Int. J. Hydrogen Energy*, 2018, **43**, 4804–4817.
2 J. Ran, J. Zhang, J. Yu, M. Jaroniec and S. Z. Qiao, Earth-abundant cocatalysts for semiconductor-based photocatalytic water splitting, *Chem. Soc. Rev.*, 2014, **43**, 7787–7812.
3 H. J. W. Li, Y. Lin, J. Duan, Q. Wen, Y. Liu and T. Zhai, Stability of electrocatalytic OER: from principle to application, *Chem. Soc. Rev.*, 2024, **53**, 10709–10740.
4 A. M. Saad, A. H. Mady, M. S. Sayed, G. Kim, M. Kim and W. K. Kim, Boosting water oxidation kinetics of $BiVO_4$ through a metal-organic co-catalyst enriched with phosphate groups (Co,Fe-NTMP): insights from LMCT mechanism and DFT study, *Appl. Catal., B*, 2024, **370**, 125163.
5 Y. Pihosh, I. Turkevych, K. Mawatari, J. Uemura, Y. Kazoe, S. Kosar, K. Makita, T. Sugaya, T. Matsui, D. Fujita, M. Tosa, M. Kondo and T. Kitamori, Photocatalytic generation of hydrogen by core-shell $WO_3/BiVO_4$ nanorods with ultimate water splitting efficiency, *Sci. Rep.*, 2015, **5**, 11141.
6 S. M. Ho-Kimura, Experimental Evidence for Photoactivated $BiVO_4$ Anodes with Enhanced Photoelectrochemical Water Oxidation, *ACS Appl. Energy Mater.*, 2024, **7**, 1902–1913.
7 J. Wiktor, I. Reshetnyak, F. Ambrosio and A. Pasquarello, Comprehensive modeling of the band gap and absorption spectrum of $BiVO_4$, *Phys. Rev. Mater.*, 2017, **1**, 022401.
8 F. F. Abdi, T. J. Savenije, M. M. May, B. Dam and R. Van De Krol, The origin of slow carrier transport in $BiVO_4$ thin film photoanodes: a time-resolved microwave conductivity study, *J. Phys. Chem. Lett.*, 2013, **4**, 2752–2757.
9 F. Li, H. Yang, Q. Zhuo, D. Zhou, X. Wu, P. L. Zhang, Z. Yao and L. Sun, A Cobalt@Cucurbit[5]uril Complex as a Highly Efficient Supramolecular Catalyst for Electrochemical and Photoelectrochemical Water Splitting, *Angew. Chem., Int. Ed.*, 2021, **60**, 1976–1985.
10 M. Balamurugan, G. Yun, K. S. Ahn and S. H. Kang, Revealing the Beneficial Effects of $FeVO_4$ Nanoshell Layer on the $BiVO_4$ Inverse Opal Core Layer for Photoelectrochemical Water Oxidation, *J. Phys. Chem. C*, 2017, **121**, 7625–7634.

© 2026 The Author(s). Published by the Royal Society of Chemistry

11 T. Jiang, W. Wang, Y. Bi, Y. Liang, J. Fu, L. Wang and Q. Zhou, Accelerating Surface Reaction Kinetics and Enhancing Bulk as well as Surface Charge Carrier Dynamics in Al/Al_2O_3-Coated $BiVO_4$ Photoanode, *Adv. Funct. Mater.*, 2024, **34**, 2403396.

12 N. Liangming, B. Dechen, L. Dongmei and Z. Yusong, Fe-Ni bimetallic-modified bismuth vanadate: a synergistic photocatalyst for CO_2 reduction, *J. Environ. Chem. Eng.*, 2025, **13**, 117760.

13 F. Yu, F. Li, T. Yao, J. Du, Y. Liang, Y. Wang, H. Han and L. Sun, Fabrication and Kinetic Study of a Ferrihydrite-Modified $BiVO_4$ Photoanode, *ACS Catal.*, 2017, **7**, 1868–1874.

14 X. Xiong, N. H. Wong, L. Ernawati, J. Sunarso, X. Zhang, Y. Jin, D. Han, C. Wu, B. Yu, X. Yang, Y. Wang, G. Chen and J. Yao, Revealing the enhanced photoelectrochemical water oxidation activity of Fe-based metal-organic polymer-modified $BiVO_4$ photoanode, *J. Colloid Interface Sci.*, 2023, **644**, 533–545.

15 C. Xia, Y. Li, M. Je, J. Kim, S. M. Cho, C. H. Choi, H. Choi, T. H. Kim and J. K. Kim, Nanocrystalline Iron Pyrophosphate-Regulated Amorphous Phosphate Overlayer for Enhancing Solar Water Oxidation, *Nano-Micro Lett.*, 2022, **14**, 209.

16 R. Altieri, M. Crisci, D. Schlettwein, B. Smarsly, F. Lamberti, T. Gatti and M. Wang, Autodrop-Enabled Aqueous Deposition of $BiVO_4$–$FePO_4$ Photoanodes for Stable Water Splitting, *Adv. Mater. Technol.*, 2025, **10**, e00672.

17 T. N. Jahangir, N. Mahar, M. G. Ahmed, N. M. Alakel, A. Al-Ahmed, A. A. Al-Saadi and T. A. Kandiel, V_2CT_x MXene suppresses V^{5+} dissolution and boosts the stability and performance of $BiVO_4$ for solar water splitting, *J. Mater. Chem. A*, 2025, **13**, 7860–7870.

18 S. Pinilla, J. Coelho, K. Li, J. Liu and V. Nicolosi, Two-dimensional material inks, *Nature Research*, 2022, **7**, 717–735.

19 M. Pogorielov, K. Smyrnova, S. Kyrylenko, O. Gogotsi, V. Zahorodna and A. Pogrebnjak, MXenes—a new class of two-dimensional materials: structure, properties and potential applications, *Nanomaterials*, 2021, **11**, 3412.

20 V. Myndrul, E. Coy, N. Babayevska, V. Zahorodna, V. Balitskyi, I. Baginskiy, O. Gogotsi, M. Bechelany, M. T. Giardi and I. Iatsunskyi, MXene nanoflakes decorating ZnO tetrapods for enhanced performance of skin-attachable stretchable enzymatic electrochemical glucose sensor, *Biosens. Bioelectron.*, 2022, **207**, 114141.

21 C. An, D. Di Dong, S. Wu, L. Gao, X. Chen, P. Jiao, Q. Deng, J. Li and N. Hu, MXene-based Materials for Water Splitting: Synthesis and Modification, *Chem.–Asian J.*, 2023, **18**, e202300429.

22 K. Raj, R. Jhala, S. Sujai, B. Pattanayak, J. Singh, P. Kumar, M. Kaladhar, R. Singh, Y. Bisht and A. Gautam, A comprehensive review on the MXene-based catalysts for hydrogen generation via water splitting processes, *J. Mol. Struct.*, 2026, **1349**, 143534.

23 Z. Guo, J. Zhou, L. Zhu and Z. Sun, MXene: a promising photocatalyst for water splitting, *J. Mater. Chem. A*, 2016, **4**, 11446–11452.

24 N. Hao, Y. Wei, J. Wang, Z. Wang, Z. Zhu, S. Zhao, M. Han and X. Huang, In situ hybridization of an MXene/TiO_2/NiFeCo-layered double hydroxide composite for electrochemical and photoelectrochemical oxygen evolution, *RSC Adv.*, 2018, **8**, 20576–20584.

25 T. Y. Shuai, Q. N. Zhan, H. M. Xu, Z. J. Zhang and G. R. Li, Recent developments of MXene-based catalysts for hydrogen production by water splitting, *Green Chem.*, 2023, **25**, 1749–1789.

26 T. M. Cheng, Y. R. Wang, Y. H. Chiu, C. Kongvarhodom, M. Saukani, S. Yougbaré, H. M. Chen and L. Y. Lin, Boosting Photoelectrochemical Catalytic Ability of Bismuth Vanadate toward Water Oxidation via Synergistic Surface Defect Engineering and MXene-Assisted Charge Transport, *ACS Omega*, 2025, **10**, 40557–40566.

27 A. Lys, I. Gnilitskyi, E. Coy, M. Jancelewicz, O. Gogotsi and I. Iatsunskyi, Highly regular laser-induced periodic silicon surface modified by MXene and ALD TiO_2 for organic pollutants degradation, *Appl. Surf. Sci.*, 2023, **640**, 158336.

28 S. Zhong, B. Kang, X. Cheng, P. Chen and B. Fang, Construction of a Co-MOF/MXene/$BiVO_4$ Composite Photoanode for Efficient Photoelectrochemical Water Splitting, *ACS Sustain. Chem. Eng.*, 2024, **12**, 1233–1246.

29 A. R. Razafintsalama, R. P. Mishra, M. K. Sahoo, M. Mrinalini, B. Sahoo, P. Ravelonandro and Y. S. Chaudhary, Efficient Photocatalytic Reduction of Hexavalent Chromium by $BiVO_4$-Decorated MXene Photocatalysts and Their Charge Carrier Dynamics, *Langmuir*, 2023, **39**, 12725–12739.

30 J. A. Abarca, M. Molera, I. Merino-Garcia, G. Díaz-Sainz, A. Irabien, J. Solla-Gullón, C. Fàbrega, T. Andreu and J. Albo, Electrodeposited $BiVO_4$-based photoanodes for an energy-efficient photo-assisted CO_2-to-formate conversion, *Chem. Eng. J.*, 2025, **514**, 163348.

31 J. A. Abarca, I. Merino-Garcia, G. Díaz-Sainz, M. Perfecto-Irigaray, G. Beobide, A. Irabien and J. Albo, Fabrication and optimization of perovskite-based photoanodes for solar-driven CO_2 photoelectroreduction to formate, *Catal. Today*, 2024, **429**, 114505.

32 I. Merino-Garcia, S. Crespo, M. Perfecto-Irigaray, G. Beobide, A. Irabien and J. Albo, Tailoring multi-layered $BiVO_4$/WO_3 photoanodes for an efficient photoelectrochemical gas-phase solar water splitting, *Catal. Today*, 2024, **432**, 114581.

33 J. A. Abarca, G. Díaz-Sainz, I. Merino-Garcia, G. Beobide, J. Albo and A. Irabien, Optimized manufacturing of gas diffusion electrodes for CO_2 electroreduction with automatic spray pyrolysis, *J. Environ. Chem. Eng.*, 2023, **11**, 109724.

34 P. Liu, J. Yi, R. Bao and H. Zhao, Construction of MXene–$BiVO_4$–FeOOH composite photoanode with ultra-low onset potential: performance, DFT calculation and mechanism, *Mater. Today Chem.*, 2022, **23**, 100747.

35 L. Ling, C. Yuan, Q. Xu, T. Li, M. Zhu and C. Zhai, Directional charge separation on 2D/2D $BiVO_4$/MXene for the enhanced photoelectrochemical detection of oxytetracycline antibiotic in water, *Surf. Interfaces*, 2023, **36**, 102483.

© 2026 The Author(s). Published by the Royal Society of Chemistry

36 S. P. Ratnayake, J. Ren, J. Van Embden, C. F. McConville and E. Della Gaspera, SILAR deposition of bismuth vanadate photoanodes for photoelectrochemical water splitting, *J. Mater. Chem. A*, 2021, **9**, 25641–25650.
37 M. R. d. S. Pelissari, N. F. Azevedo Neto, L. P. Camargo and L. H. Dall'Antonia, Characterization and Photo-Induced Electrocatalytic Evaluation for $BiVO_4$ Films Obtained by the SILAR Process, *Electrocatalysis*, 2021, **12**, 211–224.
38 R. Altieri, F. Schmitz, M. Schenker, F. Boll, L. Rebecchi, P. Schweitzer, M. Crisci, I. Kriegel, B. Smarsly, D. Schlettwein, F. Lamberti, T. Gatti and M. Wang, Development of an automated SILAR method for the sustainable fabrication of $BiOI/TiO_2$ photoanodes, *Energy Adv.*, 2024, **3**, 2564–2574.
39 E. Aydin, J. K. El-Demellawi, E. Yarali, F. Aljamaan, S. Sansoni, A. ur Rehman, G. Harrison, J. Kang, A. El Labban, M. De Bastiani, A. Razzaq, E. Van Kerschaver, T. G. Allen, O. F. Mohammed, T. Anthopoulos, H. N. Alshareef and S. De Wolf, Scaled deposition of $Ti_3C_2T_x$ MXene on Complex Surfaces: Application Assessment as Rear Electrodes for Silicon Heterojunction Solar Cells, *ACS Nano*, 2022, **16**, 2419–2428.
40 K. Hantanasirisakul, M. Q. Zhao, P. Urbankowski, J. Halim, B. Anasori, S. Kota, C. E. Ren, M. W. Barsoum and Y. Gogotsi, Fabrication of $Ti_3C_2T_x$ MXene Transparent Thin Films with Tunable Optoelectronic Properties, *Adv. Electron. Mater.*, 2016, **2**, 1600050.
41 S. Adomaviciute-Grabusove, A. Popov, S. Ramanavicius, V. Sablinskas, K. Shevchuk, O. Gogotsi, I. Baginskiy, Y. Gogotsi and A. Ramanavicius, Monitoring $Ti_3C_2T_x$ MXene Degradation Pathways Using Raman Spectroscopy, *ACS Nano*, 2024, **18**, 13184–13195.
42 R. Mirabal-Rojas, O. Depablos-Rivera, S. M. Thalluri, J. C. Medina, M. Bizarro, J. Perez-Alvarez, S. E. Rodil and A. Zeinert, Effect of the KOH chemical treatment on the optical and photocatalytic properties of $BiVO_4$ thin films, *Appl. Phys. A: Mater. Sci. Process.*, 2016, **122**, 325.
43 N. T. Huyen, T. V. Ha Luu, T. Le and H. P. Dang, Structure–property–performance correlation in $BiVO_4$ photoanodes synthesized by intensity-tuned pulse electrodeposition, *Nanoscale Adv.*, 2025, **7**, 7182.
44 D. Caus, K. Berent, K. Mech, A. Naumov, M. Marciszko-Wiąckowska and A. Podborska, Comparative Studies on Synthesis Methods of $BiVO_4$ for Photoelectrochemical Applications, *Molecules*, 2025, **30**, 3818.
45 Z. Zhang and H. Karimi-Maleh, Label-free electrochemical aptasensor based on gold nanoparticles/titanium carbide MXene for lead detection with its reduction peak as index signal, *Adv. Compos. Hybrid Mater.*, 2023, **6**, 68.
46 D. T. Bulut, Exploring the dual role of $BiVO_4$ nanoparticles: unveiling enhanced antimicrobial efficacy and photocatalytic performance, *J. Sol-Gel Sci. Technol.*, 2025, **114**, 198–222.
47 Z. Wu, H. Zong, B. Fu and Z. Zhang, MXene with controlled surface termination groups for boosting photoelectrochemical water splitting, *J. Mater. Chem. A*, 2022, **10**, 24793–24801.
48 D. W. Wang and S. Das Sarma, Resonant Raman scattering by charge-density and single-particle excitations in semiconductor nanostructures: a generalized interband-resonant random-phase-approximation theory, *Phys. Rev. B: Condens. Matter Mater. Phys.*, 2002, **65**, 125322.
49 F. M. Römer, U. Wiedwald, T. Strusch, J. Halim, E. Mayerberger, M. W. Barsoum and M. Farle, Controlling the conductivity of Ti_3C_2 MXenes by inductively coupled oxygen and hydrogen plasma treatment and humidity, *RSC Adv.*, 2017, **7**, 13097.
50 Y. Wang and P. M. A. Sherwood, Iron(III) Phosphate ($FePO_4$) by XPS, *Surf. Sci. Spectra*, 2002, **9**, 99–105.
51 J. Yang, E. Ascrizzi, M. Cattelan, M. Nalesso, L. Cielo, P. Matvija, F. Sedona, A. M. Ferrari and S. Agnoli, Atomic-Scale View of Water Chemistry on Nanostructured Iron Oxide Films, *Nano Lett.*, 2024, **24**, 12552–12559.
52 M. Lamers, W. Li, M. Favaro, D. E. Starr, D. Friedrich, S. Lardhi, L. Cavallo, M. Harb, R. Van De Krol, L. H. Wong and F. F. Abdi, Enhanced Carrier Transport and Bandgap Reduction in Sulfur-Modified $BiVO_4$ Photoanodes, *Chem. Mater.*, 2018, **30**, 8630–8638.
53 J. Yang, M. Chao, Q. Zhao, J. Li and G. Liu, Ultrathin TiO_2 passivation layer prepared by ALD significantly enhances PEC performance of $BiVO_4/NiCo_2O_4$ photoanodes, *J. Alloys Compd.*, 2025, **1024**, 180186.
54 S. N. S. Nasir, N. A. Mohamed, M. A. Tukimon, M. F. M. Noh, N. A. Arzaee and M. A. M. Teridi, Direct extrapolation techniques on the energy band diagram of $BiVO_4$ thin films, *Phys. B*, 2021, **604**, 412719.
55 W. Bai, Y. Zhou, G. Peng, J. Wang, A. Li and P. F. X. Corvini, Engineering efficient hole transport layer Ferrihydrite-MXene on $BiVO_4$ photoanodes for photoelectrochemical water splitting: work function and conductivity regulated, *Appl. Catal., B*, 2022, **315**, 121606.
56 G. Li, Z. He, H. Li, G. Du, W. Li, S. Ma, T. Shi, D. Chen and Y. Li, Amorphous Double Cocatalyst Enhanced $BiVO_4$ Photoanode for Efficient Solar-Driven Water Splitting, *ACS Appl. Mater. Interfaces*, 2025, **17**, 45836–45846.
57 S. Cheng, Y. Cheng, T. Zhou, S. Li, D. Xie and X. Li, Enhanced Photoelectrochemical Performance of $BiVO_4$ Photoanodes Co-Modified with Borate and $NiFeO_x$, *Micromachines*, 2025, **16**, 866.
58 G. Righi, J. Plescher, F. P. Schmidt, R. K. Campen, S. Fabris, A. Knop-Gericke, R. Schlögl, T. E. Jones, D. Teschner and S. Piccinin, On the origin of multihole oxygen evolution in haematite photoanodes, *Nat. Catal.*, 2022, **5**, 888–899.
59 P. Liao and E. A. Carter, Optical Excitations in Hematite (α-Fe_2O_3) via Embedded Cluster Models: A CASPT2 Study, *J. Phys. Chem. C*, 2011, **115**, 20795–20805.
60 P. Vecchi, A. Piccioni, R. Mazzaro, M. Mazzanti, V. Cristino, S. Caramori and L. Pasquini, Charge Separation Efficiency in $WO_3/BiVO_4$ Photoanodes with CoFe Prussian Blue Catalyst Studied by Wavelength-Dependent Intensity-Modulated Photocurrent Spectroscopy, *Sol. RRL*, 2022, **6**, 2200108.
61 J. Cui, M. Daboczi, Z. Cui, M. Gong, J. Flitcroft, J. Skelton, S. C. Parker and S. Eslava, $BiVO_4$ Photoanodes Enhanced

© 2026 The Author(s). Published by the Royal Society of Chemistry

with Metal Phosphide Co-Catalysts: Relevant Properties to Boost Photoanode Performance, *Small*, 2024, **20**, 2306757.
62 X. Zhang, H. Li, W. Kong, H. Liu, H. Fan and M. Wang, Reducing the surface recombination during light-driven water oxidation by core-shell $BiVO_4$@Ni:FeOOH, *Electrochim. Acta*, 2019, **300**, 77–84.
63 D. A. Panova, G. I. Tselikov, G. I. Tselikov, G. A. Ermolaev, G. A. Ermolaev, A. V. Syuy, A. V. Syuy, D. S. Zimbovskii, D. S. Zimbovskii, O. O. Kapitanova, O. O. Kapitanova, D. I. Yakubovsky, A. B. Mazitov, A. B. Mazitov, I. A. Kruglov, I. A. Kruglov, A. A. Vyshnevyy, A. A. Vyshnevyy, A. V. Arsenin, A. V. Arsenin, A. V. Arsenin, V. S. Volkov and V. S. Volkov, *Opt. Lett.*, 2024, **49**, 25–28.
64 E. Berger, Z. P. Lv and H. P. Komsa, Raman spectra of 2D titanium carbide MXene from machine-learning force field molecular dynamics, *J. Mater. Chem. C*, 2023, **11**, 1311–1319.
65 K. Shevchuk, A. Sarycheva, C. E. Shuck and Y. Gogotsi, Raman Spectroscopy Characterization of 2D Carbide and Carbonitride MXenes, *Chem. Mater.*, 2023, **35**, 8239–8247.
66 A. Sarycheva and Y. Gogotsi, Raman Spectroscopy Analysis of the Structure and Surface Chemistry of $Ti_3C_2T_x$ MXene, *Chem. Mater.*, 2020, **32**, 3480–3488.
67 D. B. Lioi, G. Neher, J. E. Heckler, T. Back, F. Mehmood, D. Nepal, R. Pachter, R. Vaia and W. J. Kennedy, Electron-Withdrawing Effect of Native Terminal Groups on the Lattice Structure of $Ti_3C_2T_x$ MXenes Studied by Resonance Raman Scattering: Implications for Embedding MXenes in Electronic Composites, *ACS Appl. Nano Mater.*, 2019, **2**, 6087–6091.
68 S. R. M. Thalluri, C. Martinez-Suarez, A. Virga, N. Russo and G. Saracco, Insights from Crystal Size and Band Gap on the Catalytic Activity of Monoclinic $BiVO_4$, *Int. J. Chem. Eng. Appl.*, 2013, **4**, 305–309.

© 2026 The Author(s). Published by the Royal Society of Chemistry